

AperTO - Archivio Istituzionale Open Access dell'Università di Torino

## Ligand-Selective Photodissociation from [Ru(bpy)(4AP)4]2+: a Spectroscopic and Computational Study

**This is the author's manuscript**

*Original Citation:*

*Availability:*

This version is available <http://hdl.handle.net/2318/59536> since

*Published version:*

DOI:10.1021/ic8015436

*Terms of use:*

Open Access

Anyone can freely access the full text of works made available as "Open Access". Works made available under a Creative Commons license can be used according to the terms and conditions of said license. Use of all other works requires consent of the right holder (author or publisher) if not exempted from copyright protection by the applicable law.

(Article begins on next page)



# UNIVERSITÀ DEGLI STUDI DI TORINO

***This is an author version of the contribution published on:***

*Questa è la versione dell'autore dell'opera:*

*Inorganic Chemistry, 48 (4), 2009, 10.1021/ic8015436*

***The definitive version is available at:***

*La versione definitiva è disponibile alla URL:*

*<http://pubs.acs.org/doi/abs/10.1021/ic8015436>*

# Ligand-Selective Photodissociation from $[\text{Ru}(\text{bpy})(4\text{AP})_4]^{2+}$ : a Spectroscopic and Computational Study

Luca Salassa,<sup>†</sup> Claudio Garino,<sup>‡</sup> Giovanni Salassa,<sup>‡</sup> Carlo Nervi,<sup>‡</sup> Roberto Gobetto,<sup>‡\*</sup> Carlo Lamberti,<sup>‡</sup> Diego Gianolio,<sup>‡</sup> Ranieri Bizzarri,<sup>§</sup> Peter J. Sadler<sup>†\*</sup>

<sup>†</sup> *Department of Chemistry, University of Warwick, Gibbet Hill Road, Coventry CV4 7AL, United Kingdom*

<sup>‡</sup> *Department of Chemistry IFM and NIS centre of Excellence, University of Turin, via P. Giuria 7, 10125 Turin, Italy*

<sup>§</sup> *Laboratorio NEST, Scuola Normale Superiore di Pisa, Complesso San Silvestro, Piazza San Silvestro 12, 56127, Pisa, Italy*

## Abstract

The new complex  $[\text{Ru}(\text{bpy})(4\text{AP})_4]^{2+}$  (**1**), where bpy = 2,2'-bipyridine and 4AP = 4-aminopyridine, undergoes selective photodissociation of two 4APs upon light excitation of the MLLCT band at 510 nm. The photoproducts of the reaction are *mer*- $[\text{Ru}(\text{bpy})(4\text{AP})_3(\text{H}_2\text{O})]^{2+}$  (**2a**) and *trans*-(4AP)- $[\text{Ru}(\text{bpy})(4\text{AP})_2(\text{H}_2\text{O})_2]^{2+}$  (**3a**). Photodissociation occurs in two consecutive steps with quantum yields of  $\phi_1 = (6.1 \pm 1.0) \cdot 10^{-3}$  and  $\phi_2 = (1.7 \pm 0.1) \cdot 10^{-4}$ , respectively. Complex **1** was characterized by combined spectroscopic and theoretical techniques. EXAFS experiments at the Ru K-edge (22117 eV) of **1** in aqueous solution gave Ru–N distances of  $2.09 \pm 0.01$  Å. Photoproducts were characterized by electronic spectroscopy, 1D and 2D NMR and mass spectrometry. Singlet and triplet excited states of **1** were studied by DFT and TDDFT for characterizing the optical properties of the complex. In the singlet state, <sup>1</sup>MC (metal-centered) dissociative states lie 0.65 eV above the main <sup>1</sup>MLLCT transition in the visible region of the UV-vis absorption spectrum. In the triplet state, the energy difference between these states is not reduced. However, potential energy curves of singlet and triplet excited states of **1** along the Ru–N(*axial* 4AP) and Ru–N(*equatorial* 4AP) stretching coordinate show that the release of the first 4AP may occur from the triplet state by mixing of <sup>3</sup>MLLCT and <sup>3</sup>MC dissociative states. This mixing is favored when the Ru–N(*equatorial* 4AP) bond is elongated, explaining the formation of the photoproduct **2a**.

---

\* Corresponding author. E-mail: Roberto.gobetto@unito.it.

## Introduction

Photoactivable metal complexes offer unique features for new applications in medicinal chemistry. It has been shown recently how selective activation of prodrugs or controlled delivery of small biologically active molecule can be achieved by using this class of compounds.<sup>1-6</sup> In both cases the key step is the light-induced dissociation of one (or more) coordinated ligand and the subsequent coordination of a solvent molecule.<sup>7</sup> This process can trigger a specific interaction between the metal complex and a target macromolecule or simply cause the release of the ligand (e. g., neuroactive compound) in a selected tissue. Thus, time and spatial control are, in principle, possible when photoactivable compounds are used. Further advantages can be introduced by the use of low-energy irradiation, such as visible light or two-photon excitation, which reduce cell damage and have higher tissue penetration.<sup>8,9</sup>

Recently, Sadler *et al.* prepared platinum anticancer derivatives that exhibit cytotoxicity only when irradiated with UV light.<sup>1-6</sup> In the case of *trans,trans,trans*-[Pt(N<sub>3</sub>)<sub>2</sub>(OH)<sub>2</sub>(NH<sub>3</sub>)(py)],<sup>1</sup> the drug was 80-times more potent than cisplatin. The complex *cis*-(Cl,Cl)-[Ru(terpy)(NO)(Cl)<sub>2</sub>]Cl (where terpy = 2,2':6',2''-terpyridine) is also cytotoxic when irradiated,<sup>10</sup> as a result of the efficient photodissociation of the toxic NO radical. In the field of drug delivery, Etchenique *et al.* studied the *in vitro* photorelease of 4-aminopyridine from the complex [Ru(bpy)<sub>2</sub>(4AP)<sub>2</sub>]<sup>2+</sup> (where bpy = 2,2'-bipyridine and 4AP = 4-aminopyridine) upon excitation with 490-nm light and evaluated the 4AP-induced effect on cellular membrane potentials using neurophysiological techniques.<sup>3</sup>

The nature of singlet and triplet excited states strictly controls the excitation wavelength, the mechanism of ligand dissociation, and the photodissociation yield. Therefore, development of metal-based photoactivable drugs requires a deep understanding of such properties. Density functional theory (DFT) and time-dependent DFT are fundamental tools for the study of excited state properties of metal complexes<sup>11-20</sup> and their photochemistry.<sup>21-29</sup>

In this paper, we report the synthesis and characterization of the new photoactivable complex [Ru(bpy)(4AP)<sub>4</sub>]<sup>2+</sup> (**1**). Complex **1** was design to allow the dissociation of two ligands from the coordination sphere of the ruthenium center, and thus give rise to a di-substituted product, which, in principle, is able to give stable cross-linked DNA-adducts. The characterization of the photoproducts *mer*-[Ru(bpy)(4AP)<sub>3</sub>(H<sub>2</sub>O)]<sup>2+</sup> (**2a**) and *trans*-(4AP)-[Ru(bpy)(4AP)<sub>2</sub>(H<sub>2</sub>O)<sub>2</sub>]<sup>2+</sup> (**3a**) was achieved by a combination of spectroscopy and computational techniques. Finally, we report a detailed TDDFT study on the photodissociation mechanism for release of the first 4AP ligand in **1**.

## Experimental Section

**Materials and Methods.** All solvents were analytical reagent grade and purified according to established procedures.<sup>30</sup> Ruthenium(III) chloride hydrate was purchased from Lancaster and used as received. Sodium perchlorate, tetrabutylammonium chloride, 4-aminopyridine, and  $\alpha$ -phellandrene were purchased from Aldrich and used as received without further purification. 2,2'-Bipyridine, obtained from Aldrich, was purified by crystallization from hexane and dried under vacuum over P<sub>2</sub>O<sub>5</sub>. [Ru(bpy)(p-cymene)(Cl)]Cl was prepared according to the literature.<sup>31</sup> Triple-distilled water was used routinely. All the reactions involving metal complexes were performed in an argon atmosphere. NMR spectra were recorded on a JEOL EX 400 spectrometer (<sup>1</sup>H operating frequency 400 MHz) and on a Bruker Advance 600 (<sup>1</sup>H operating frequency 600 MHz) with chemical shifts referenced to residual protons in the solvent. UV-Vis absorption spectra were measured with a DR LANGE CADAS 200 spectrophotometer. Room-temperature emission spectra, as well as luminescence lifetimes, were recorded using a HORIBA Jobin Yvon IBH Fluorolog-TCSPC spectrofluorimeter. Luminescence lifetimes were determined by time-correlated single-photon counting. Samples were excited with nanosecond pulses of 297 nm light (repetition rate 1 MHz) generated by a NanoLED pulsed diode. The emission data were collected using a spectral bandwidth of 10 nm. The data were collected into 2048 channels with up to 10000 counts in the peak channel. The sample was maintained

at 20°C in an automated sample chamber (F-3004 Peltier Sample Cooler from Horiba Jobin Yvon IBH) for ambient temperature measurements. Emission decay data were analyzed using the software DAS6 (TCSPC Decay Analysis Software). Decay curves were fit by reconvolution of the time-dependent profile of the light source. Assessment of the best fit was based on the parameter  $\chi^2$  and the distribution of weighted residual along the zero line. Mass spectra were recorded using an XCT PLUS electrospray ionization ion trap (ESI-IT) mass spectrometer (Agilent, Milan Italy). Samples were dissolved in water or in water/acetonitrile (95:5) mixture. The scan range was  $m/z$  200–800.

**Photodissociation Study.** [Ru(bpy)(4AP)<sub>4</sub>][ClO<sub>4</sub>]<sub>2</sub> was dissolved in 100 mM phosphate buffered saline (PBS) and adjusted to pH 7.4. A 1.5 mL aliquot of the solution was placed in a 1-cm quartz cuvette (Hellma Optik GmbH, Jena, Germany) equipped with a 3-mm magnetic stirrer. The solution was irradiated under vigorous stirring by using the 488-nm line beam of a argon-gas laser (Coherent, Santa Clara, CA, USA). Illumination intensities were selected from the 0.1–1 W/cm<sup>2</sup> range. At different times, the absorption spectrum of the solution was measured by means of a Jasco 550 spectrophotometer (Jasco, Tokyo, Japan). Photokinetic absorption curves at 488 nm were fit by a written code running on *IgorPro 5.0* (Wavemetrics, Eugene, OR).

NMR tubes containing solutions of **1** were irradiated in a dark chamber with 510-nm light from a 450 W xenon CW lamp. The irradiation intensity on the sample at the wavelength employed was approximately 5–6 mW/cm<sup>2</sup> and irradiation times ranged from 2 to 5 h. NMR spectra were recorded immediately after irradiation. A similar procedure was adopted for the ESI mass experiments. Aqueous solutions of **1** were irradiated for 2h and then mass spectra were run either in pure water or in a 5% acetonitrile/water mixture. Isotopic patterns of all assigned species were confirmed by simulation using the online software at <http://winter.group.shef.ac.uk/chemputer/isotopes.html>.

**EXAFS Measurements and Data Analysis.** X-ray absorption experiments, at the Ru K-edge (22117 eV), were performed at the BM29 of the ESRF facility (Grenoble, France).<sup>32</sup> The white beam was monochromatized using a Si(111) double crystal; harmonic rejection was performed by detuning the crystals at 20% of the rocking curve. Energy calibration was at 23222 eV using a Rh metal foil. An EXAFS cell, specifically devoted to liquid samples, was filled with an aqueous solution of [Ru(bpy)(4AP)<sub>4</sub>][Cl]<sub>2</sub> just below the saturation limit (10 mM). Because of Ru dilution, EXAFS spectra were collected in fluorescence mode, by means of a 13-element germanium monolithic detector, collecting the Ru K <sub>$\alpha$ 1-3</sub> fluorescence lines in the 18500–19500 eV range. To limit the flux of elastically-scattered photons (21800–23500 eV), a Mo filter (acting as a low-band pass filter with threshold at 20000 eV) was inserted between the sample and the fluorescence detector. This insertion allowed the sample-to-detector distance to be minimized (thus maximizing the solid angle seen by the detector and consequently the Ru K <sub>$\alpha$ 1-3</sub> fluorescence photons). The intensity of the incident beam was monitored by an ionization chamber. The beam transmitted through the sample passed further through a second ionization chamber, resulting in a transmission EXAFS spectrum characterized by edge jump of 0.03. The XANES part of the spectra was acquired with an energy step of 1 eV and an integration time of 2 s/point. The EXAFS part of the spectra was collected with a variable sampling step in energy, resulting in  $\Delta k = 0.03 \text{ \AA}^{-1}$ , up to  $18 \text{ \AA}^{-1}$ , with an integration time that linearly increases with  $k$  from 2 to 20 s/point to account for the low signal-to-noise ratio at high  $k$  values. The extraction of the  $\chi(k)$  function was performed using Athena programs.<sup>33</sup> For both samples, three consecutive EXAFS spectra were collected, resulting in three  $\mu\text{x}$  spectra (obtained by integrating the counts of the 13 elements of the detector), and corresponding  $\chi(k)$  functions were averaged before data analysis. Analogously, the three EXAFS spectra, simultaneously collected in transmission mode, were extracted and corresponding  $\chi(k)$  functions averaged before data analysis, resulting in the  $k^2\chi(k)$  function (see Figure in the Supporting Information). The quality of the  $\chi(k)$  function obtained from the transmitted spectrum, impressive for a sample with 0.05 of edge jump, is due to the high homogeneity of the liquid sample and on the high stability of BM29 beamline. EXAFS data analysis performed on the two sets of data resulted, within experimental errors, in the same values for all optimized parameters (not reported for brevity) and,

consequently, the fluorescence and transmission data sets have been averaged (see figure in the Supporting Information). The same data analysis has been repeated for the final averaged data set (vide infra Figure 1 and Table 2), resulting in optimized parameters compatible with those obtained in the two previous analyses but characterized by smaller error bars. EXAFS data analysis has been performed using the Artemis software.<sup>33</sup> Phase and amplitude functions were calculated by FEFF6 code<sup>34</sup> using as input the structure obtained from DFT calculations. Phase and amplitudes have been successfully checked with [Ru(bpy)<sub>3</sub>](Cl)<sub>2</sub> as a model compound, measured in transmission mode with the same sampling procedure described for the liquid sample (only two spectra collected). For each sample the averaged  $k^2\chi(k)$  function was Fourier transformed in the  $\Delta k = 2.00\text{--}18.00 \text{ \AA}^{-1}$  interval. The fits were performed in  $R$  space in the  $\Delta R = 1.00\text{--}5.00 \text{ \AA}$  range ( $2\Delta k\Delta R/\pi > 40$ ). Because of the complexity of the structure, 180 single scattering (SS) and multiple scattering (MS) paths contribute to the overall EXAFS signal. By excluding the paths having an amplitude smaller than 5% of the most intense one (the Ru–N SS path around 2.11  $\text{\AA}$  for the closest bpy unit), 74 paths have been included in the fit. To limit the number of optimized variables, all paths have been optimized with the same amplitude factor ( $S_0^2$ ) and with the same energy shift parameter ( $\Delta E$ ). Moreover, both the 4APs and bpy ligands have been considered as rigid molecules for the only degree of freedom is a radial translation along the corresponding Ru–N axis. The two 4AP ligands are assumed to behave in the same way, and the same has been inferred for the bpy rings. Consequentially, the only two structural parameters optimized in the fit are  $R_{\text{Ru–N(4AP)}}$  and  $R_{\text{Ru–N(bpy)}}$ , being the lengths of all the other 74 paths computed from the  $R_{\text{Ru–N(4AP)}}$  and  $R_{\text{Ru–N(bpy)}}$  values, according to geometrical constraints imposed by the rigidity of the 4AP and bpy entities. When the inter-ligand vibrations of the 4AP and bpy units are neglected, only two Debye-Waller factors have been optimized,  $\sigma_{\text{Ru–N(4AP)}}$  and  $\sigma_{\text{Ru–N(bpy)}}$ , for all the paths involving 4AP or bpy atoms, respectively. MS paths involving atoms of different 4AP (or of different bpy) units have been simulated with a Debye-Waller factor of  $\sigma_{\text{MS}} = 4\sigma_{\text{Ru–N(4AP)}}$  (or of  $4\sigma_{\text{Ru–N(bpy)}}$ ); MS paths involving atoms of a 4AP and of a bpy units have been simulated with a Debye-Waller factor of  $\sigma_{\text{MS}} = \sigma_{\text{Ru–N(4AP)}} + \sigma_{\text{Ru–N(bpy)}} + 2[\sigma_{\text{Ru–N(4AP)}}\sigma_{\text{Ru–N(bpy)}}]^{1/2}$ .

**Computational Details.** All calculations were performed with the *Gaussian 03* (G03) program<sup>35</sup> employing the DFT method, the Becke three-parameter hybrid functional,<sup>36</sup> and Lee–Yang–Parr’s gradient-corrected correlation functional (B3LYP).<sup>37</sup> The LanL2DZ basis set<sup>38</sup> and effective core potential were used for the Ru atom, and the 6-311G\*\* basis set<sup>39</sup> was used for all other atoms. Geometry optimizations of **1** in the ground state ( $S_0$ ) and lowest-lying triplet state ( $T_1$ ) were performed in the gas phase, and the nature of all stationary points was confirmed by normal mode analysis. The conductor-like polarizable continuum model method (CPCM)<sup>40–42</sup> with water as solvent was used to calculate the electronic structure and the excited states of **1** in solution. A total of 32 singlet excited states and their corresponding oscillator strengths were determined with a TDDFT<sup>43,44</sup> calculation. The computational results are summarized in Table 3, where only electronic transitions with an oscillator strength value ( $f$ ) higher than 0.05 are reported. The electronic distribution and the localization of the singlet excited states were visualized using the electron density difference maps (EDDMs).<sup>45</sup> *GaussSum 1.05*<sup>46</sup> was used for EDDMs calculations and for the electronic spectrum simulation. The equation employed by the program to calculate the theoretical spectrum and the extinction coefficients is based on gaussian convolution and is reported in the open source code of the program (available at <http://gausssum.svn.sf.net/viewvc/gausssum/Trunk/src/gausssum/>). The full-width at half maximum (fwhm) value used for the simulated spectrum was obtained by averaging experimental values (3100  $\text{cm}^{-1}$  for the band centered at 510 nm, and 3600  $\text{cm}^{-1}$  for the one at 300 nm). Triplet excited states were calculated by TDDFT starting either from the ground-state geometry or the lowest-lying triplet state geometry.<sup>47,48</sup> In the first case restricted B3LYP was used, while in the latter both restricted and unrestricted B3LYP was employed. The emission energy of complex **1** was evaluated both employing the  $\Delta\text{SCF}$  approach<sup>11</sup> and TDDFT at the  $T_1$  geometry.

Calculations of proton magnetic shielding tensors ( $\sigma$ ) for **1**, **2a**, **2b** and **3a–c** were performed at the B3LYP/LanL2DZ(6-311++G\*\*) level using the GIAO<sup>49</sup> method implemented in *Gaussian 03*. The  $\sigma$  values

were converted into proton chemical shifts  $\delta$ , relative to the magnetic shielding of tetramethylsilane computed with the corresponding basis set. Detailed results of these calculations are reported in the Supporting Information.

**Ru-4AP Photodissociation calculations.** The effects of Ru–N(4AP) bond elongation on singlet and triplet excited states were studied computationally by TDDFT. Starting from the minimum geometry, Ru–N(*axial* 4AP) and Ru–N(*equatorial* 4AP) distances were increased separately and independently by 0.1 Å. For each step the Ru–N bond distance was frozen and the geometry of molecule allowed to relax to a stationary point. Each single geometry was then employed for calculating 32 singlet and 16 triplet excited states by TDDFT at the B3LYP/LanL2DZ(6-311++G\*\*) level. Potential energy curves (PECs) for selected singlet and triplet excited states are reported in Figures 9 and 10. This procedure as shown to be accurate, but it is worth highlighting that it is based on the assumption that ground- and excited- state geometries do not differ too much.<sup>22,29</sup>

**Synthesis of [Ru(bpy)(4AP)<sub>4</sub>][ClO<sub>4</sub>]<sub>2</sub> ([1][ClO<sub>4</sub>]<sub>2</sub>).** The complex [Ru(bpy)(p-cymene)(Cl)]Cl<sup>31</sup> (150 mg) and 4AP (300 mg, ratio about 1:10) were dissolved in water and stirred at reflux for 2 days. The mixture was cooled down under nitrogen and precipitated using sodium perchlorate. (*Perchlorate salts of metal complexes with organic ligands are potentially explosive. They should be handled with great care in small quantities*). The purple precipitate was collected and washed with hexane and diethyl ether. Yield: 78 %; <sup>1</sup>H-NMR (acetone-d<sub>6</sub>, ppm): 8.88 (d, J<sub>HH</sub> = 5.7 Hz, 2H), 8.61 (d, J<sub>HH</sub> = 8.2 Hz, 2H), 8.05 (t, J<sub>HH</sub> = 8.0 Hz, J<sub>HH</sub> = 1.3 Hz, 2H), 7.91 (d, J<sub>HH</sub> = 7.3 Hz, 4H), 7.69 (t, J<sub>HH</sub> = 5.9 Hz, J<sub>HH</sub> = 1.5 Hz, 2H), 7.29 (d, J<sub>HH</sub> = 7.0 Hz, 4H), 6.82 (d, J<sub>HH</sub> = 7.2 Hz, 4H), 6.44 (d, J<sub>HH</sub> = 7.0 Hz, 4H), 6.34 (s, broad), 6.12 (s, broad). <sup>13</sup>C-NMR (acetone-d<sub>6</sub>, ppm): 159.8, 155.4, 155.3, 154.5, 153.3, 152.9, 135.8, 126.9, 123.8, 111.1, 110.7. MS: *m/z* 733 [1][ClO<sub>4</sub>]<sup>+</sup>. Elem anal. Calcd for C<sub>30</sub>H<sub>32</sub>N<sub>10</sub>O<sub>8</sub>Cl<sub>2</sub>Ru: C, 43.28; H, 3.87; N, 16.82. Found: C, 43.42; H, 3.73; N, 16.69.

In order to achieve a greater solubility in water, the chloride salt of **1** was also prepared by metathesis with tetrabutylammonium chloride. The solubility of the chloride complex is increased from 5–6 mg/ml to 15–20 mg/ml, and no significant variation of the photophysical properties was observed.

**Synthesis of [Ru(bpy)(4AP)<sub>4</sub>]Cl<sub>2</sub> ([1][Cl]<sub>2</sub>).** The ClO<sub>4</sub><sup>–</sup> salt was dissolved into a minimum amount of acetone. Drops of a saturated solution of tetrabutylammonium chloride in acetone were added until total precipitation of the chloride salt was achieved. The precipitate was washed several times with acetone and dried. <sup>1</sup>H NMR (D<sub>2</sub>O, ppm): 8.63 (d, J<sub>HH</sub> = 5.37 Hz, 2H), 8.28 (d, J<sub>HH</sub> = 8.05 Hz, 2H), 7.85 (m, 6H), 7.43 (t, J<sub>HH</sub> = 6.30 Hz, 2H), 7.22 (d, J<sub>HH</sub> = 5.86 Hz, 4H), 6.65 (d, J<sub>HH</sub> = 5.74 Hz, 4H), 6.26 (d, J<sub>HH</sub> = 5.74 Hz, 4H). <sup>13</sup>C NMR (D<sub>2</sub>O, ppm): 159.5, 154.8, 154.7, 154.5, 153.3, 152.9, 135.8, 126.4, 123.5, 111.4, 111.0.

## Results and Discussion

**DFT Geometry Features.** Geometry optimization of the complex **1** was performed with the B3LYP method as described in the Computational Details section. The complex has a pseudooctahedral structure. In the ground-state geometry (S<sub>0</sub>), the Ru–N(bpy) bond distance is 2.11 Å. The axial 4AP N atoms are at 2.17 and 2.18 Å from the ruthenium atom, and the equatorial 4AP N atoms are both at 2.20 Å. The bpy N–Ru–N bite angle is small, 77.8°; the N–Ru–N between the equatorial 4APs is slightly larger than 90° (91.1°), while the axial N–Ru–N angle is 179.1°, with the 4AP ligands slightly bent towards the diimine ligand. In the lowest-lying triplet geometry (T<sub>1</sub>), **1** shows significantly shorter Ru–N(bpy) bonds (2.07 Å); both Ru–N(*equatorial* 4AP) bonds are equally elongated (2.23 Å), while one *axial* 4AP N atom is now 2.18 Å from the Ru atom and the other is at 2.12 Å. Longer distances for the equatorial 4AP ligands are consistent with a more labile bond and correlate with the release of the first 4AP from this position.

Geometry optimization of all possible mono-aqua and diaqua derivatives (Scheme 1 and Table 1) was performed as well. In **2a** the Ru–N(*axial* 4AP) distances do not differ significantly from **1**. Ru–N(bpy) bonds are shortened to 2.06 Å (*trans* to H<sub>2</sub>O) and 2.09 Å (*trans* to 4AP). The Ru–O bond is 2.26 Å and the equatorial 4AP nitrogen is 2.18 Å from the metal center. Also for **2b**, Ru–N(bpy) distances are almost

identical to those of complex **1**. *Equatorial* 4AP bonds are slightly shorter (2.19 Å), while the *axial* 4AP bond is reduced to 2.11 Å. The Ru–O bond is 2.26 Å.

### Scheme 1

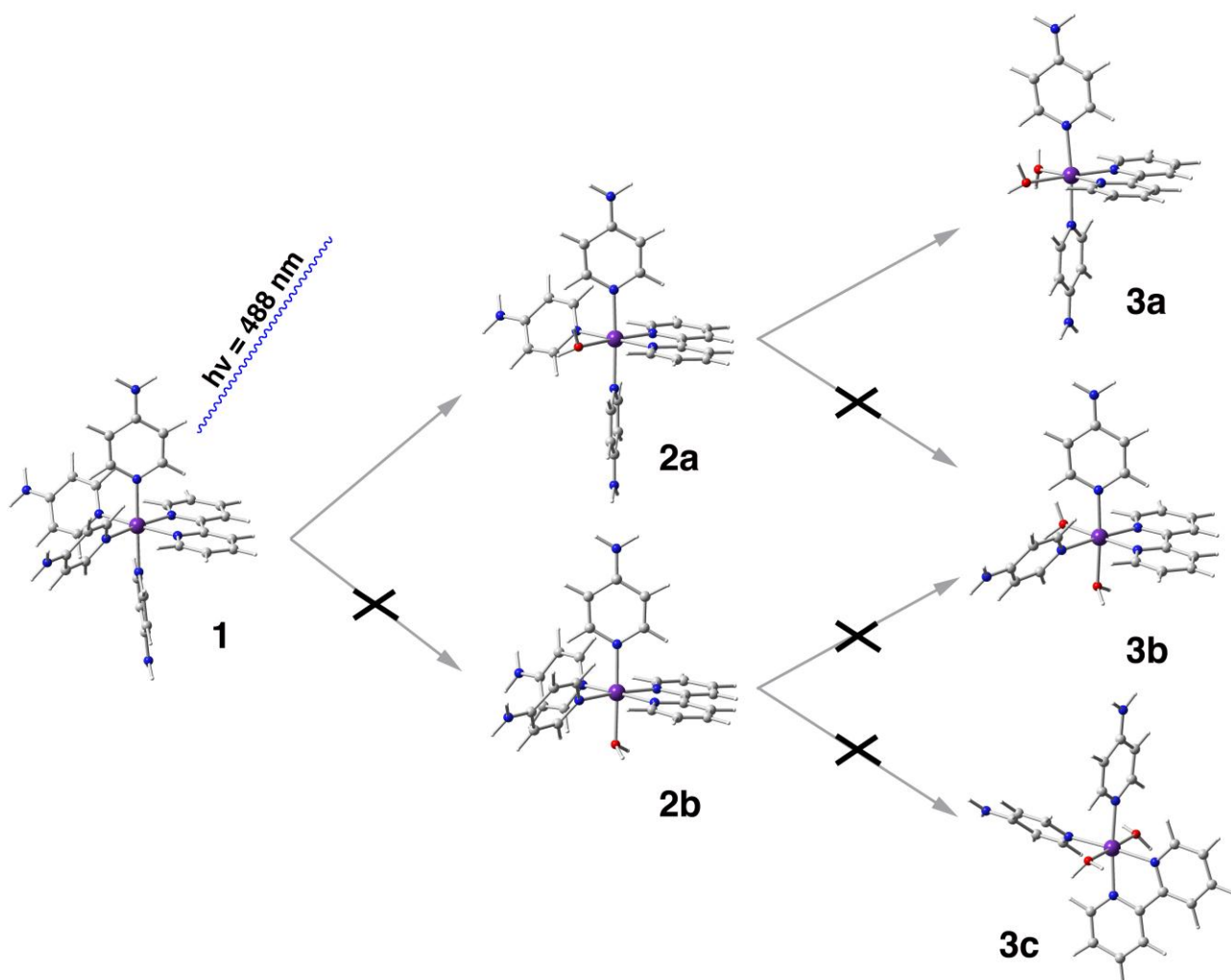


**Table 1.** Selected bond distances (Å) for all optimized complexes.<sup>a</sup>

	Ru–N(bpy)	Ru–N(bpy)	Ru–N(4AP)	Ru–N(4AP)	Ru–N(4AP)	Ru–N(4AP)
<b>1</b> ( $S_0$ )	2.1134	2.114	2.201	2.202	2.177	2.174
<b>1</b> ( $T_1$ )	2.069	2.070	2.229	2.229	2.122	2.181
	Ru–N(bpy)	Ru–N(bpy)	Ru–N(4AP)	Ru–N(4AP)	Ru–N(4AP)	Ru–OH <sub>2</sub>
<b>2a</b>	2.065	2.093	2.182	2.159	2.171	2.264
<b>2b</b>	2.116	2.120	2.192	2.189	2.114	2.266
	Ru–N(bpy)	Ru–N(bpy)	Ru–N(4AP)	Ru–N(4AP)	Ru–OH <sub>2</sub>	Ru–OH <sub>2</sub>
<b>3a</b>	2.054	2.048	2.158	2.155	2.255	2.268
<b>3b</b>	2.070	2.199	2.171	2.108	2.251	2.258
<b>3c</b>	2.127	2.115	2.165	2.171	2.196	2.199

<sup>a</sup> Red and blue indicate ligands in the equatorial and axial position, respectively

In the case of **3a**, Ru–N(bpy) bonds are reduced to 2.05 Å, the axial 4APs are at 2.16 Å from the Ru center, and the water molecules are at 2.25 and 2.27 Å. In the isomer **3b**, Ru–N(bpy) bonds are 2.07 and 2.10 Å, the



4AP trans to bpy is at 2.17 Å, while the other is at 2.11 Å. Ru–O bonds are 2.25 and 2.26 Å. Finally, in **3c** Ru–N(bpy) bonds are longer (2.11 and 2.13 Å), Ru–N(*equatorial* 4AP) bonds are 2.17 Å and the water ligands in axial position are tightly bound to the metal center (2.20 Å).

**EXAFS.** EXAFS spectra from two samples were recorded on beamline BM29 of the ESRF facility (Grenoble, France); the first was a 1 mM aqueous solution of the model compound [Ru(bpy)<sub>3</sub>][Cl]<sub>2</sub>, and the second a 1 mM aqueous solution of **1**[Cl]<sub>2</sub>. The quality of the fit obtained for [Ru(bpy)<sub>3</sub>][Cl]<sub>2</sub> can be observed in the spectrum reported in Figure 1A. Looking to the optimized parameters, we obtain a negligible energy shift, an  $S_0^2$  equal to unit within the experimental uncertainty, a Debye-Waller Factor of 0.0028 Å<sup>2</sup> and a Ru–N distance of  $2.056 \pm 0.004$  Å, that is, within experimental uncertainty, comparable to the value obtained from similar EXAFS experiments ( $2.066 \pm 0.017$ ).<sup>50-52</sup> The quality of the fit was further confirmed by the very low values of the associated errors and by the low correlations among the four fitted parameters:  $S_0^2/\sigma = 0.75$  and  $\Delta E/R_{\text{Ru-N}} = 0.71$  (all other correlations are below 0.25 in absolute value).

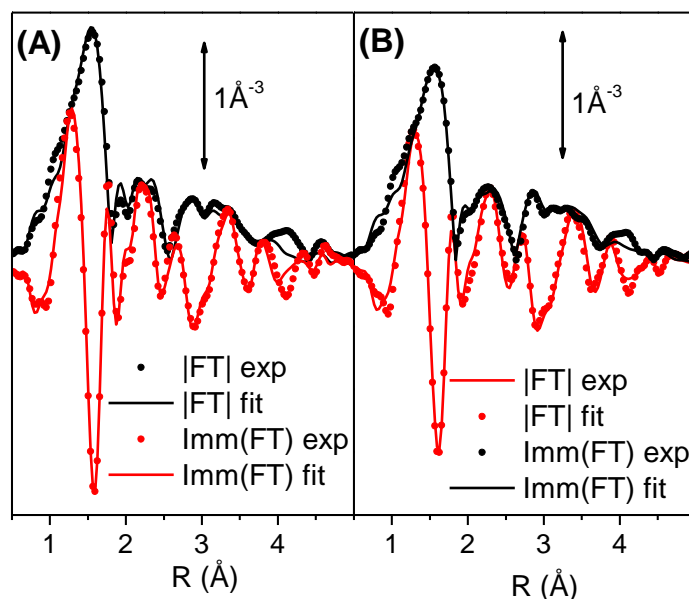


**Figure 1.** Comparison between experimental (dotted lines) and corresponding best fits (solid lines) for [Ru(bpy)<sub>3</sub>][Cl]<sub>2</sub> (A), and [Ru(bpy)(4AP)<sub>4</sub>][Cl]<sub>2</sub> (B) samples. In black are reported the modulus and in red the imaginary parts. For values of the parameters optimized in the fits, see Table 2.

**Table 2. Summary of the parameters optimized in the fitting<sup>a</sup> of the EXAFS data (Figure 1)**

	[Ru(bpy) <sub>3</sub> ][Cl] <sub>2</sub>	[Ru(bpy)(4AP) <sub>4</sub> ][Cl] <sub>2</sub>
$N_{\text{ind}}$	40	40
$N_{\text{fit}}$	4	6
$R_{\text{factor}}$	0.039	0.031
$S_0^2$	$1.05 \pm 0.05$	$1.03 \pm 0.06$
$\Delta E$ (eV)	$-0.1 \pm 0.4$	$-0.0 \pm 0.4$
$R_{\text{Ru-N(bpy)}} (\text{Å})$	$2.056 \pm 0.004^b$	$2.09 \pm 0.01^c$
$\sigma_{\text{Ru-N(bpy)}} (\text{Å}^2)$	$0.0028 \pm 0.0004$	$0.003 \pm 0.001$
$R_{\text{Ru-N(4AP)}} (\text{Å})$	-	$2.09 \pm 0.01^d$
$\sigma_{\text{Ru-N(4AP)}} (\text{Å}^2)$	-	$0.005 \pm 0.001$

<sup>a</sup> The fits were performed in R-space in the 1.0–5.0 Å range over  $k^2$ -weighted FT of the  $\chi(k)$  functions performed in the 2.0–18.0 Å<sup>-1</sup> interval. A single  $\Delta E_0$  and a single  $S_0^2$  have been optimized for all SS and MS paths. Non optimized parameters are recognizable by the absence of corresponding error bars. Optimized bond distances are compared to the average values obtained from DFT calculations.

<sup>b</sup> In the literature, the  $R_{\text{Ru-N(bpy)}}$  distance in [Ru(bpy)<sub>3</sub>](Cl)<sub>2</sub> has been reported to be: (i)  $2.066 \pm 0.017$  Å from EXAFS data in Ref. 44a; (ii) in the 2.05–2.064 Å range from XRD studies in Refs 44b and 44c; (iii) 2.106 Å from DFT calculations, this work.

<sup>c</sup> 2.114 Å from DFT calculations, this work.

<sup>d</sup> 2.188 Å from DFT calculations, this work.

Once the EXAFS of the  $[\text{Ru}(\text{bpy})_3][\text{Cl}]_2$  model compound was correctly reproduced, the spectrum of the  $\mathbf{1}[\text{Cl}]_2$  sample was simulated. As for the model compound, values of  $\Delta E$  and  $S_0^2$  compatible with 0 and 1, respectively, were obtained. Because the bpy unit contributes almost twice as much as the 4AP ligands to the high distance paths, corresponding distances and Debye-Waller factors were determined with better precision. Within the experimental uncertainty, which is very small in both cases, the Debye-Waller factor of the bpy unit is the same for the  $[\text{Ru}(\text{bpy})_3][\text{Cl}]_2$  and  $\mathbf{1}[\text{Cl}]_2$  samples (Table 2). In accordance with the lower mass, the 4AP units of the latter sample exhibit a Debye-Waller factor that is almost twice that of bpy. According to the DFT calculations, the insertion of four 4AP units, substituting two bpy ligands, results in an increase of the  $R_{\text{Ru-N}(\text{bpy})}$  distance by 0.008 Å. Although borderline within the uncertainty of the EXAFS technique, the experimental results confirm a bond stretching of  $0.03 \pm 0.01$  Å, that is in qualitative agreement with the elongation predicted by the calculations. The Ru–N(4AP) distance is  $2.09 \pm 0.01$  Å, which is 0.09 Å shorter than the value predicted by calculations (Table 2). Curiously, the optimized  $R_{\text{Ru-N}(\text{bpy})}$  and  $R_{\text{Ru-N}(4\text{AP})}$  distances become equivalent taking account of the associated errors.<sup>53</sup> The higher correlation among parameters occurs for  $R_{\text{Ru-N}(4\text{AP})}/R_{\text{Ru-N}(\text{bpy})} = -0.82$ ,  $S_0^2/\sigma_{\text{Ru-N}(4\text{AP})} = 0.64$ ,  $\sigma_{\text{Ru-N}(4\text{AP})}/\sigma_{\text{Ru-N}(\text{bpy})} = -0.62$ , and  $\Delta E/R_{\text{Ru-N}(4\text{AP})} = 0.57$ ; all other correlations are below 0.25 in absolute value. In summary, it is concluded that the EXAFS data analysis fully confirms the overall structure optimized in the DFT calculations; the experimental Ru–N distances are systematically shorter by a few hundredths of an angstrom.

**Electronic Absorption Spectrum and Singlet Excited State for Complex 1.** Experimental and theoretical absorption spectra of complex **1** in water are reported in Figure 2. TDDFT was employed for calculating 32 singlet excited states starting from the gas-phase optimized geometry. Selected states are reported in Table 3 and in Figure 3 (black energy levels). The solvent effect was taken into account with the CPCM method.

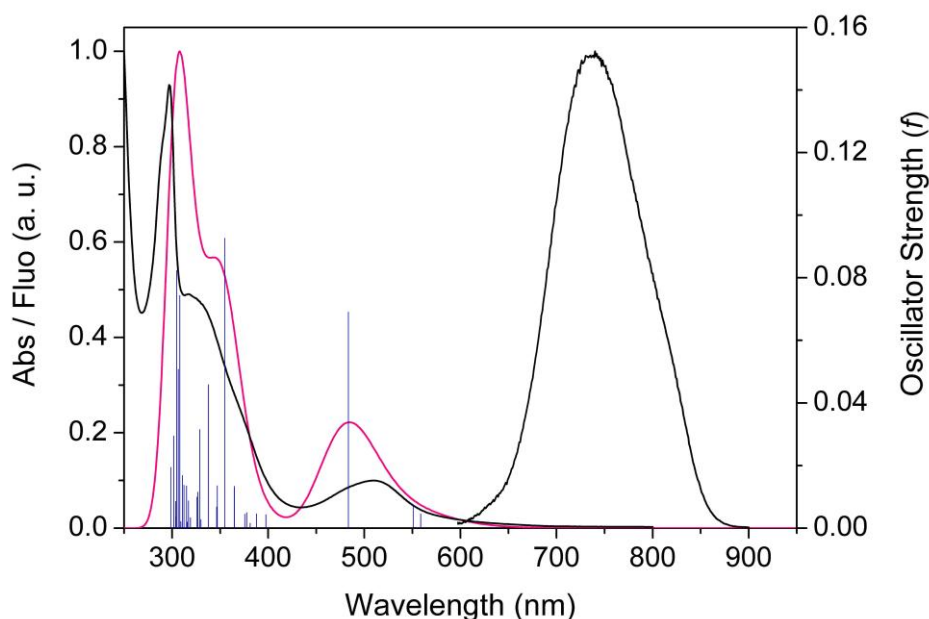


**Figure 2.** Calculated (magenta line) and experimental (black line) absorption and emission (black line) spectra of **1** in  $\text{H}_2\text{O}$ . The excited states are shown as vertical bars with heights equal to the oscillator strength values. The theoretical curve was obtained using the program *GussSum 1.05*.

Despite a very good agreement between experimental and simulated UV–vis spectra, the band centered at 510 nm in the experimental electronic spectrum is blue-shifted by DFT calculation, which correctly reproduces the extinction coefficient of the band. The calculated energy is at 2.56 eV (484 nm) with an oscillator strength of 0.068. This  $^1\text{MLLCT}$  state originates from a nearly pure one-electron migration and, as shown by the computed EDDM (**S3**, Figure 3), there is electron density migration from  $\pi^*$  orbitals of an axial 4AP to bpy. The two transitions at lower energy contribute to this band despite their small oscillator strength values ( $< 0.002$ ). They both have  $^1\text{MLLCT}$  character and display density migration from  $\pi^*$  orbitals of 4APs (two equatorial and one axial). A series of mixed  $^1\text{MLCT/MC}$  (metal-centered) states (**S4–S8**) are

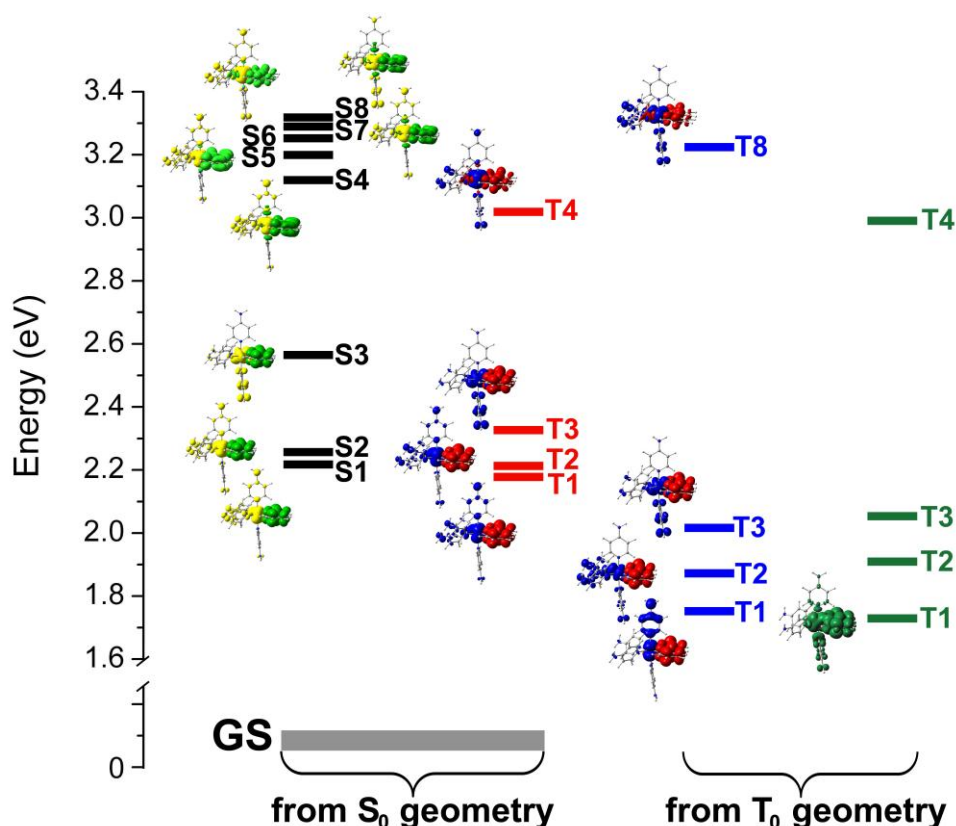


**Figure 3.** Singlet and triplet excited-state energy level diagram for complex **1**. Black bars represent singlet excited states obtained by TDDFT at the ground-state geometry; red and blue bars are triplet excited states calculated by TDDFT at the ground-state and lowest-lying triplet state geometries, respectively; green bars represent triplet states calculated using the UKS method and unrestricted TDDFT. EDDMs of singlet and triplet transitions are reported, as well as the countour plot of the spin density (dark green) of the lowest-lying triplet state geometry of complex **1** (isovalue 0.0004). In the case of singlet transitions, yellow indicates a decrease in electron density and light green an increase, while for triplets blue indicates a decrease in electron density and red an increase. (S1–S3:  $^1\text{MLCT}$ ; S4–S8:  $^1\text{MC}/^1\text{MLCT}$ ; T1–T3:  $^3\text{MLCT}$ ; T4:  $^3\text{MC}/^3\text{MLCT}$ ; T1–T3:  $^3\text{MLCT}$ ; T4:  $^3\text{MC}/^3\text{MLCT}$ ; T1:  $^3\text{MLCT}$ ; T2 and T3:  $^3\text{MC}/^3\text{LC}$ ; T4:  $^3\text{LMCT}$ ).

present in the region between 397 and 375 nm (3.12–3.30 eV). Such states play a decisive role in the ligand photodissociation mechanism because of their dissociative nature (see below). The shoulder at 330 nm is due to MLCT states of Ru  $\rightarrow$  bpy character. No pure ligand-based states seem to be present from the computational results. The UV band around 300 nm is formed by electronic transitions from the metal to 4AP ligands; electron density is transferred from the metal orbitals to the  $\pi^*$  orbitals of either axial or equatorial 4APs. Computed oscillator strength ( $f$ ) values for the UV bands are underestimated compared to the experimental spectrum (see Table 3). Changes in pH do not affect noticeably the absorption properties of **1**.

Solvatochromism can be adopted as a quick qualitative and indirect measure of the extent of backdonation from the metal center to the diimine ligand in complexes with the general formula  $[\text{M}(\text{L})_4(\alpha\text{-diimine})]$ .<sup>54,55</sup> This parameter can determine the charge-transfer nature of an excited state. The higher the backbonding, the lower the solvatochromic effect. In the case of  $[\text{Ru}(\text{bpy})(4\text{AP})_4]^{2+}$  changing from dichloromethane and acetone solutions to water, a 10 nm blue shift is observed. Hence, good backdonation must be postulated in order to justify such a limited effect.<sup>54</sup> The small bpy bite angle of **1** correlates well with such a feature.

**Emission Spectrum and Triplet Excited States for Complex 1.** Upon excitation of the  $^1\text{MLCT}$  band at 510 nm, complex **1** gives a low-intensity unstructured emission centered at about 750 nm ( $13.6 \times 10^3 \text{ cm}^{-1}$ ). The emission lifetime was measured in water at room temperature to be 8.2 ns. Short lifetimes have already been reported by other authors in complexes having a  $[\text{Ru}(\text{bpy})\text{L}_4]^{2+}$  structure.<sup>56–59</sup>

**Table 3. Experimental and calculated absorption and emission properties of complex 1**

$\lambda_{\text{max}}$ , nm $\epsilon$ ( $\text{M}^{-1} \text{cm}^{-1}$ )	Tr. <sup>a</sup>	Composition	Energy, eV (nm)	Oscillator Strength	Assignment
510 (4100)	<b>S3</b>	HOMO-2 $\rightarrow$ LUMO (81%)	2.56 (484)	0.068	MLLCT
330 (19900)	<b>S11</b>	HOMO-3 $\rightarrow$ LUMO (37%) HOMO-2 $\rightarrow$ LUMO+1 (16%) HOMO-1 $\rightarrow$ LUMO+1 (17%)	3.50 (354)	0.091	MLLCT
298 (38300)	<b>S26</b>	HOMO-2 $\rightarrow$ LUMO+3 (17%) HOMO-1 $\rightarrow$ LUMO+3 (15%) HOMO-1 $\rightarrow$ LUMO+4 (10%) HOMO-2 $\rightarrow$ LUMO+4 (9%) HOMO-1 $\rightarrow$ LUMO+6 (9%) HOMO-1 $\rightarrow$ LUMO+11 (9%)	4.02 (308)	0.073	MLCT (4AP)
	<b>S27</b>	HOMO-2 $\rightarrow$ LUMO+4 (14%) HOMO-2 $\rightarrow$ LUMO+6 (32%) HOMO-1 $\rightarrow$ LUMO+4 (12%) HOMO-1 $\rightarrow$ LUMO+6 (32%)	4.04 (306)	0.049	MLCT (4AP)
	<b>S28</b>	HOMO-3 $\rightarrow$ LUMO+3 (15%) HOMO-2 $\rightarrow$ LUMO+5 (20%) HOMO-2 $\rightarrow$ LUMO+6 (16%) HOMO-1 $\rightarrow$ LUMO+5 (21%) HOMO-1 $\rightarrow$ LUMO+6 (12%) HOMO-1 $\rightarrow$ LUMO+11 (9%)	4.07 (305)	0.081	MLCT (4AP)
$\lambda_{\text{em}}$ , nm ( $10^3 \text{ cm}^{-1}$ )	$\lambda_{\text{ASCF}}$ , nm ( $10^3 \text{ cm}^{-1}$ )	$\lambda_{\text{TDDFT}}$ , nm ( $10^3 \text{ cm}^{-1}$ )	$\phi$	$\tau$ (ns)	Assignment
750 (13.3)	714 (14.0)	708 (14.1)	0.002	8.2	MLLCT

<sup>a</sup> Tr. = Transition (Tr. indicates the transition number as obtained in the TDDFT calculation output).

Two approaches were used for studying the nature of the emitting triplet state and other high-energy triplets. The first method consisted in a restricted TDDFT calculation of triplet excited-state energies from the singlet ground-state geometry  $S_0$  (Figure 3: red energy levels) and the lowest-lying triplet state geometry  $T_1$  (Figure 3: blue energy levels),<sup>11,60</sup> the second method was a DFT calculation on  $T_1$  employing unrestricted Kohn-Sham (UKS) (Figure 3: green energy levels). The differences in excited-state energy and in electron density between the TDDFT and UKS methods are well known. Unrestricted techniques tend to give qualitatively sound energy values but incorrect densities, whereas restricted methods behave in the opposite manner. However, UKS calculation with no symmetry constraints produces satisfactory results in terms of densities as well.<sup>60</sup>

The optimized  $T_1$  geometry was also used to estimate the emission energy using TDDFT and  $\Delta\text{SCF}$  approaches.<sup>11</sup>

Using restricted TDDFT and  $S_0$ , the first four computed triplet states are 2.20–3.08 eV (563–403 nm) above the ground state. The two lowest-energy states are almost degenerate and have <sup>3</sup>MLLCT character. The third state (**T3**) is only 0.11 eV above these two states, and corresponds to the lowest-lying <sup>3</sup>MLLCT triplet obtained with the UKS method. Moreover, **T3** can be populated by intersystem crossing from **S3**. The fourth triplet state (**T4**) is the only dissociative state towards 4APs; it has higher energy with respect to the lower three states (0.75 eV) and its nature is due to the dissociative virtual orbitals that are involved in the transition (see below).

Triplet states obtained using  $T_1$  geometry have similar character, but different energies. In the case of the dissociative state **T8** (which corresponds to **T4** calculated from  $S_0$ ), the energy difference from **T3** is noticeably increased (1.10 eV).

A slightly different scenario is obtained with the UKS method. The spin density of **1** at the  $T_1$  geometry, calculated as the difference in  $\alpha$  and  $\beta$  density of the triplet state geometry, was used for describing the nature of the lowest triplet state<sup>61</sup> (Figure 3: green and blue contour plot). The surface shape leads to the conclusion that the lowest triplet excited state has <sup>3</sup>MLLCT character, involving the same *axial* 4AP that was implicated in the singlet transition centered at 510 nm (**S3**). Interestingly, the spin density surface does not match completely the density of the two SOMOs, but can be approximated by the HOMO–2 of  $S_0$  (see below) and the higher-SOMO of  $T_1$ . Approximation with SOMO orbital densities may not be sufficient for a correct representation of spin density.<sup>62–64</sup> In fact, unpaired electrons spin-polarize the electron distribution in the closed-shells, adding spin density at the position of the nuclei and leading to positive and negative spin density.<sup>65</sup> Also in the <sup>3</sup>MLLCT state, there is a limited charge-transfer character. In fact, Mulliken charge on the Ru center is only slightly reduced going from the singlet state to the triplet state (from + 0.98 to + 1.16). The  $T_1$  geometry (UKS) was employed to calculate the energy of 16 new triplet states by unrestricted TDDFT. Among them, two states are close in energy to  $T_1$ , at 0.18 and 0.32 eV. These states are mixed MC(d orbitals)/LC(4AP) states with no dissociative character towards the ligands. The third state is 1.26 eV higher in energy than  $T_1$ , and has ligand-to-metal charge-transfer character. All the other triplet states are of mixed character and have higher energy (> 1.45 eV). Endicott et al. found a similar arrangement of low lying triplet states for other  $[\text{Ru}(\text{bpy})\text{L}_4]^{2+}$  complexes.<sup>56–59</sup>

The emission energy estimated computationally for **1** is in good agreement with the experimental data.<sup>20,28</sup> The values obtained by TDDFT and by  $\Delta\text{SCF}$ <sup>11</sup> are 709 nm ( $14.1 \times 10^3 \text{ cm}^{-1}$ ) and 714 nm ( $14.0 \times 10^3 \text{ cm}^{-1}$ ), respectively.

**Photodissociation Products of  $[\text{Ru}(\text{bpy})(4\text{AP})_4]^{2+}$ .** When exposed to light,  $[\text{Ru}(\text{bpy})(4\text{AP})_4][\text{ClO}_4]_2$  was found to photodissociate and release 4AP. Indeed, the presence of free 4AP was clearly visible in the <sup>1</sup>H NMR spectrum of a solution of **1** in D<sub>2</sub>O exposed to 488 nm light ( $0.3 \text{ W/cm}^2$ ) for few minutes.

We attempted to determine the photocleavage mechanism and quantum yield of the complex under typical experimental condition to assess the potential high-resolution spatially-controlled release of photolabile compounds in living cells. We irradiated solutions of **1** in phosphate buffered saline (PBS, pH 7.4) with 488-nm laser light at various intensities (from 0.1 to  $1 \text{ W/cm}^2$ ) and monitored the optical characteristics of the solution.

Upon illumination, the solution gave rise to a general time-dependent decrease in intensity of bands in the absorption spectrum except in the 260–270 nm range, where bands for the free 4AP peak are located (Figure 4). Close examination of the visible region (400–650 nm) revealed that the photocleavage leads to a 30-nm blue shift of the lowest energy band of the Ru complex, from 510 to 480 nm (Figure 4, inset). In the same region, two nearly isosbestic points around 410 and 460 nm were detected. In Figure 4, the progression of the reaction is shown. The plots of 488 nm-absorbance vs. time at the different laser powers shed light on the nature of the photocleavage process (Figure 5). Indeed, the absorbance decays were always found to be biphasic, suggesting the presence of two consecutive dissociation reactions of 4AP. In addition, both decay phases occurred faster under higher irradiation powers, consistent with the hypothesis of light-activated dissociation (Figure 5). The quantitative kinetic treatment of a consecutive two-step photodissociation process is reported in section S2 of the Supporting Information. Global fitting of the decay curves with the numerical solution of the kinetic system [S4.8] allowed determination of the photocleavage quantum yields of the two reactions ( $\phi_1$  and  $\phi_2$ ). We found  $\phi_1 = (6.1 \pm 1.0) \times 10^{-3}$  and  $\phi_2 = (1.7 \pm 0.1) \times 10^{-4}$ . Thus, the loss of the first 4AP ligand induces a nearly 30-fold reduction in the efficiency of the photocleavage of a further 4AP molecule. Interestingly, Etchenique et al.<sup>3</sup> reported a value of ca. 0.02 for the photodissociation of 4AP at 473 nm from the  $[\text{Ru}(\text{bpy})_2(4\text{AP})_2]^{2+}$  complex. From the photocleavage quantum yields, the average



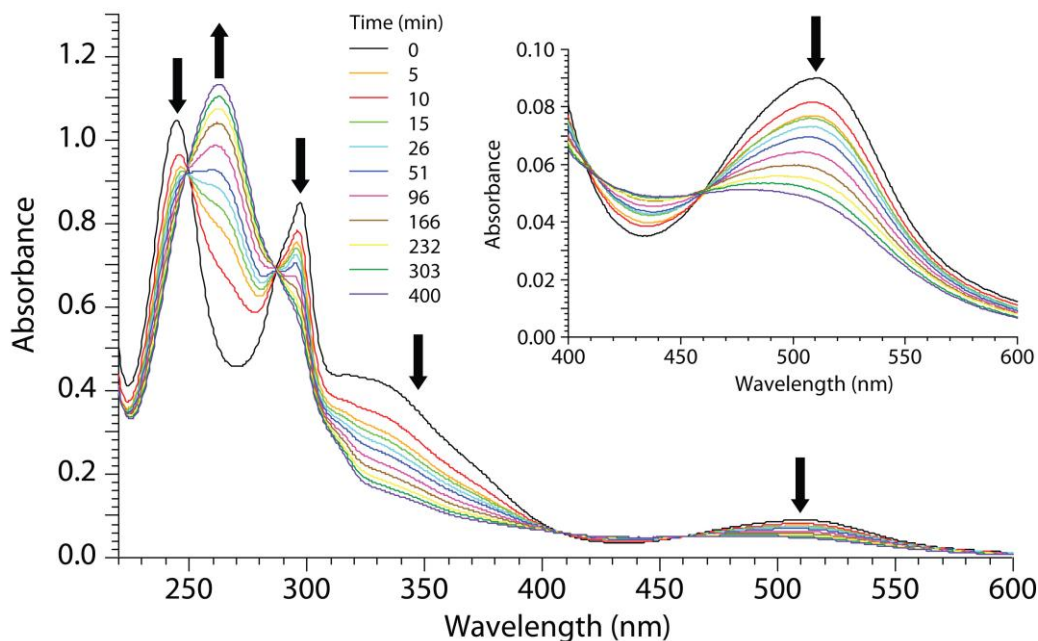


**Figure 4.** Absorption spectra of  $1[\text{ClO}_4]_2$  in PBS solution irradiated by a 488 nm  $0.1 \text{ kW/cm}^2$  laser beam for different times (see legend). Inset: enlargement of the 400-650 nm region.

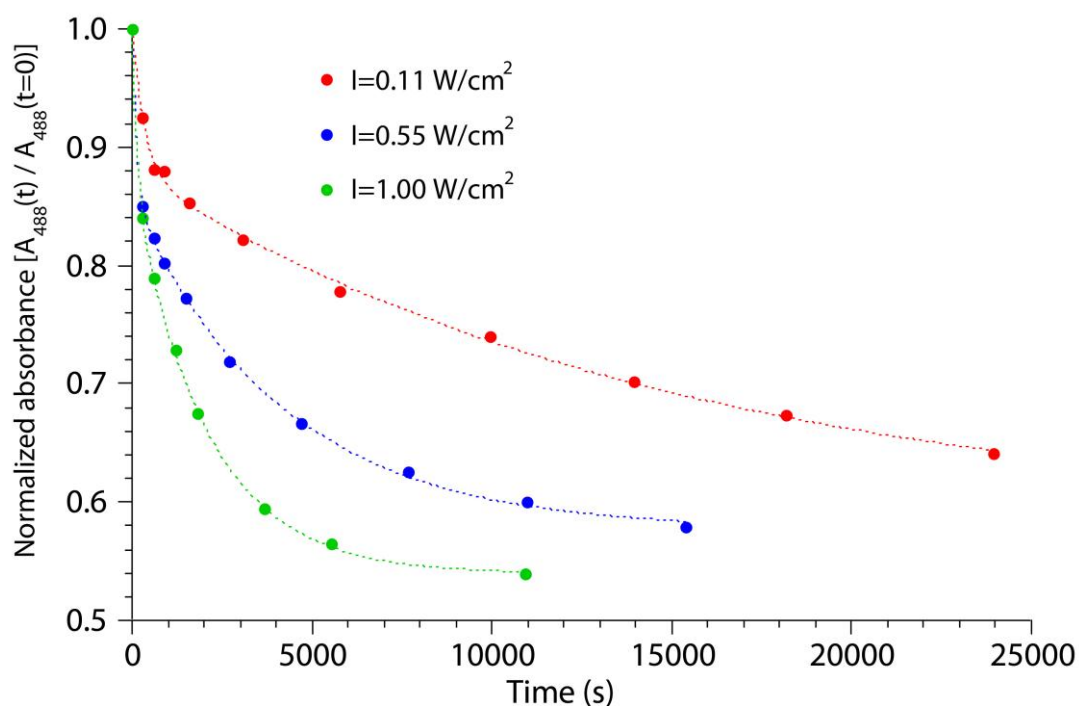


**Figure 5.** Plots of absorbance at 488 nm vs time for a PBS solution of  $1[\text{ClO}_4]_2$  irradiated at three different illumination intensities (488 nm). Dotted curves are the fits to experimental data by means of eq. S4.8 (Supporting Information).

survival times of the  $[\text{Ru}(\text{bpy})(4\text{AP})_4]^{2+}$  and  $[\text{Ru}(\text{bpy})(4\text{AP})_3(\text{H}_2\text{O})]^{2+}$  complexes in PBS solution under irradiation can be calculated according to

$$\tau = \frac{h \cdot c \cdot N_A}{2300 \cdot I \cdot \varepsilon \cdot \lambda \cdot \varphi} \quad [1]$$

where  $I$  is the illumination intensity (in  $\text{Watt/cm}^2$ ),  $h$  is Planck's constant,  $c$  is the speed of light ( $\text{cm/s}$ ),  $N_A$  is the Avogadro's number,  $\lambda$  is the illumination wavelength, and  $\varepsilon$  is the extinction coefficient at that wavelength. Assuming  $\varepsilon_{488}$  values of  $2975 \text{ M}^{-1} \cdot \text{cm}^{-1}$  and  $2530 \text{ M}^{-1} \cdot \text{cm}^{-1}$  for  $[\text{Ru}(\text{bpy})(4\text{AP})_4]^{2+}$  and  $[\text{Ru}(\text{bpy})(4\text{AP})_3(\text{H}_2\text{O})]^{2+}$ , respectively (the latter value comes from the fitting of the photoinduced decays), gives average survival times of

$$\tau_{[\text{Ru}(\text{bpy})(4\text{AP})_4]} = \frac{5.89}{I} (\mu\text{s})$$

$$\tau_{[\text{Ru}(\text{bpy})(4\text{AP})_3(\text{H}_2\text{O})]} = \frac{241.43}{I} (\mu\text{s})$$
[2]

To allow dissociation of 4AP from ruthenium with high spatial and temporal resolution, the survival times must be lower than the residence time of the complex ( $\tau_r$ ) in the waist of the light beam ( $w$ ).<sup>66</sup> For common microimaging setups, beam waists as narrow as 0.2  $\mu\text{m}$  can be obtained by means of high-numeric aperture objectives. Assuming a diffusion coefficient around 100  $\mu\text{m}^2/\text{s}$ , typical of low molecular weight molecules in a cell environment,<sup>67</sup>  $\tau_r$  is calculable from the expression<sup>66</sup>

$$\tau_r = \frac{w^2}{4D} = \frac{0.2^2 (\mu\text{m}^2)}{400 (\mu\text{m}^2 / \text{s})} = 0.1 \text{ ms}$$
[3]

Thus, from eq 2 we find that a light intensity near 60  $\text{W}/\text{cm}^2$  is required for effective release of one 4AP molecule. This intensity is easily accessible using common microimaging setups equipped with Ar laser excitation sources and high numeric aperture objectives.

**NMR Spectroscopy.** Photodissociation of **1** in  $\text{D}_2\text{O}$  solution and 22 mM NaCl aqueous solution was studied by  $^1\text{H}$  NMR spectroscopy. Both solutions give the same photoproducts upon excitation of the MLLCT band centered at 510 nm with a 450 W Xe CW lamp (Scheme 1). The data are in agreement with photocleavage experiments described in the previous section. The  $^1\text{H}$  NMR spectrum of **1** in deuterated water or sodium chloride solution (Figure 6A) has four resonances corresponding to the 8 bpy protons, and four resonances with double intensities corresponding to the 16 4AP protons. A small amount of free 4AP is present in the spectrum at 7.92 and 6.71 ppm in part due to sample manipulation in the light. The doublets at 7.73 and 6.52 ppm correspond to the ortho and meta protons of the equatorial 4APs [with respect to the  $\text{Ru}(\text{bpy})$  unit], while the doublets at 7.14 and 6.20 ppm correspond to the ortho and meta signals of the axial 4APs. This assignment was obtained from  $^1\text{H}$ – $^1\text{H}$  COSY and  $^1\text{H}$ – $^1\text{H}$  NOESY 2D NMR experiments and was confirmed by DFT-computed chemical shift values. Because of the symmetry of the complexes and the similar distances between Ru and the 4APs moieties and the bpy moiety, we used the GIAO method for predicting proton chemical shift differences of the axial and equatorial 4APs. Different magnetic shielding constant calculations were performed on **1** and its diaqua derivatives, **2a**, **2b**, and **3a–c** (data are reported in the Supporting Information). We have previously demonstrated<sup>68</sup> that this method can be valuable for assigning proton resonances when a molecular structure cannot be easily solved by 2D NMR techniques. 4APs have sharp doublets indicating that rotation is fast around the Ru–N axes on the NMR timescale at the investigated temperature (285–343 K). Ru–N(4AP) distances are, in fact, longer in the case of **1** with respect to similar Ru derivatives displaying dynamic behavior.<sup>69</sup>

Upon irradiation of a solution containing **1** in millimolar concentrations, two aqua species are formed. The most abundant species corresponds to the mono aqua derivative **2a**, while the less abundant is the diaqua complex **3a**. The proposed assignments were obtained by 1D  $^1\text{H}$  and 2D  $^1\text{H}$ – $^1\text{H}$  TOCSY experiments (Figure 7) and DFT/GIAO calculations. Figure 6B shows the  $^1\text{H}$  spectrum in 22 mM NaCl solution after 3h light irradiation with a Xe lamp. In the case of **2a**, the eight resonances observed for the bpy ligand are consistent with substitution of one 4AP trans to bpy. Also, the axial 4APs have signals which have double the integrated intensity of the equatorial 4APs. Furthermore, the chemical shifts of all 4APs of **2a** with respect to **1** are correctly assigned by DFT prediction (ortho–equatorial 4AP is the single resonance upfield). All resonances relative to **2a** are broad, indicating that solvent exchange processes and rotational motions of ligands are occurring on the NMR timescale.

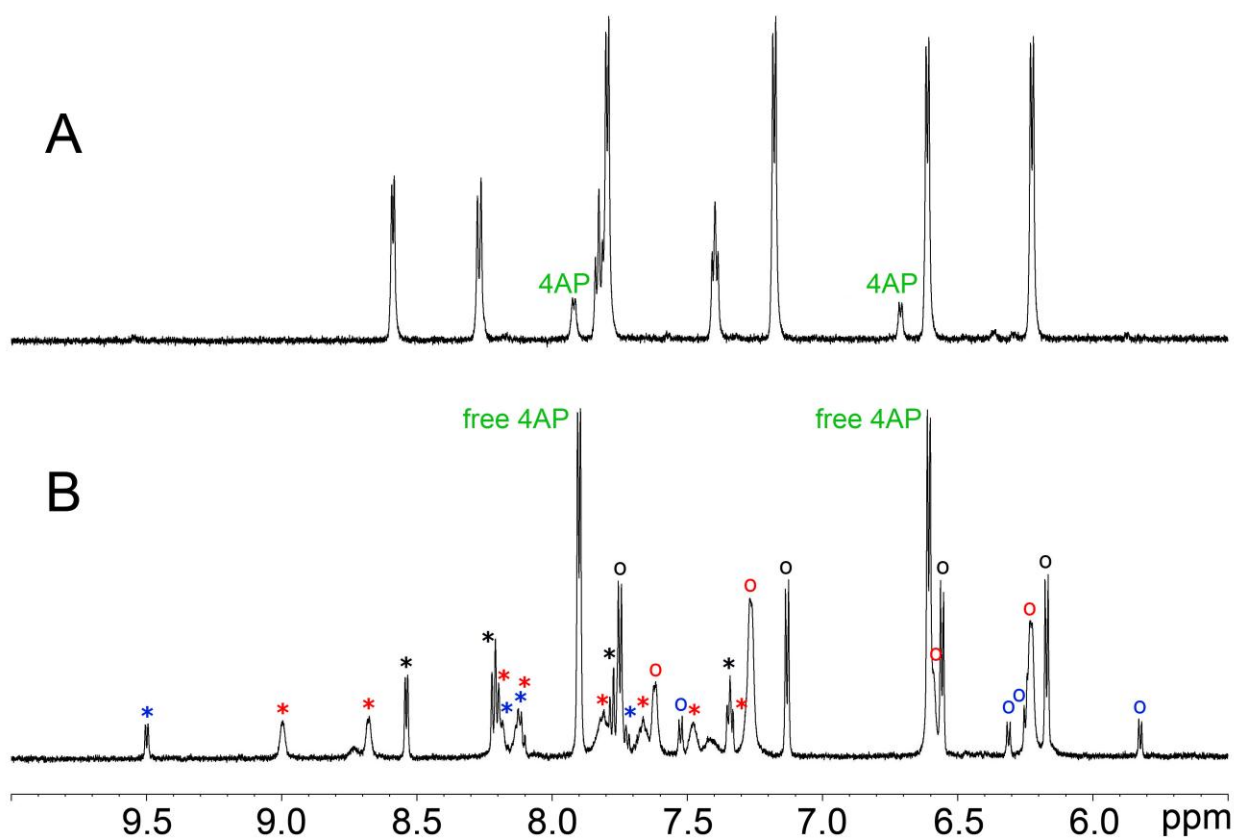


**Figure 6.**  $^1\text{H}$  NMR spectrum of **1** in NaCl 22 mM in  $\text{D}_2\text{O}$  (upper) and after 5-hour irradiation with 510-nm light (lower). In the lower  $^1\text{H}$  NMR spectrum peaks were assigned as follows: **1** (bpy \*, 4APs o); **2a** (bpy \*, 4APs o); **3a** (bpy \*, 4APs o). The lamp employed was a 450 W xenon CW lamp; light intensity on the sample was ca. 5–6 mW.

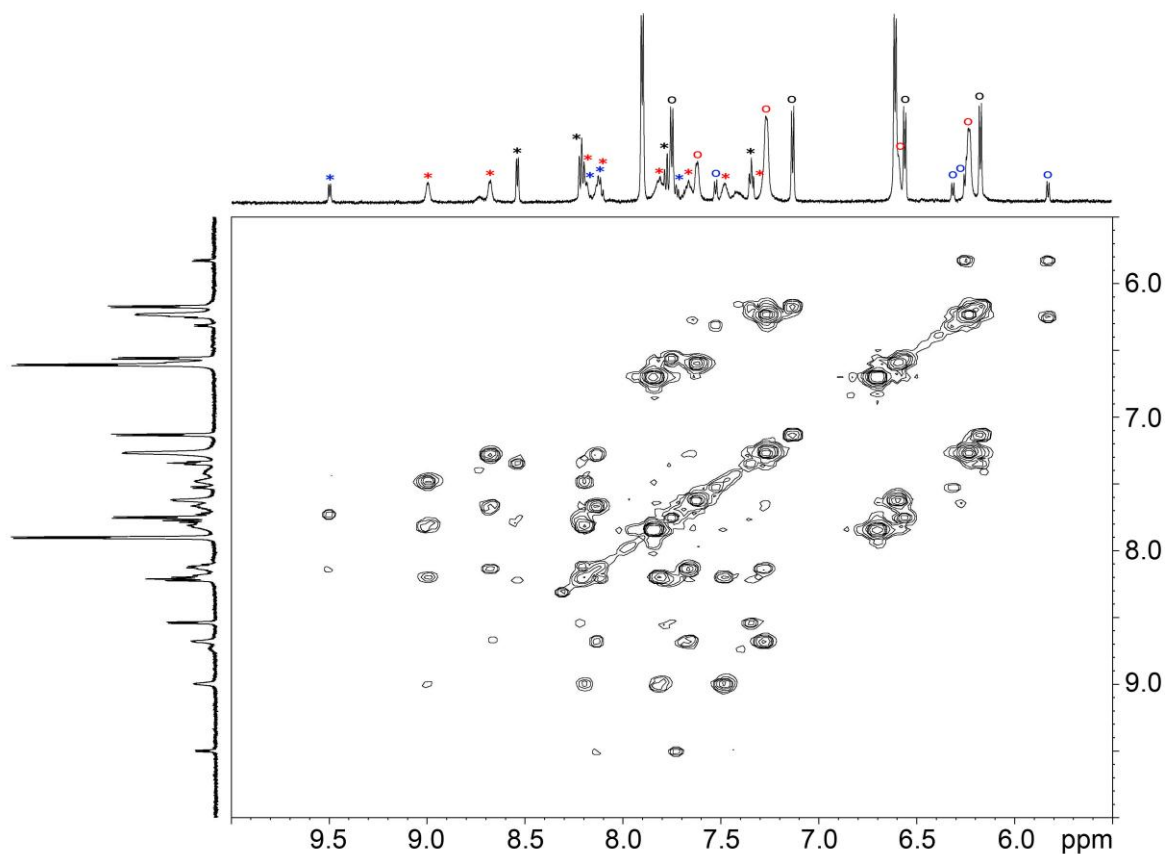


**Figure 7.** 2D  $^1\text{H}$ -TOCSY NMR spectrum of **1** in NaCl 22 mM in  $\text{D}_2\text{O}$ . In 1D  $^1\text{H}$  NMR spectrum peaks were assigned as follows: **1** (bpy \*, 4APs o); **2a** (bpy \*, 4APs o); **3a** (bpy \*, 4APs o).



As demonstrated, the release of a second 4AP is more difficult. After prolonged exposure to 510 nm light, the *cis* (equatorial) diaqua derivative **3a** is formed, among all other possible diaqua isomers. This species is generally less abundant than **2a** because of the low irradiation power of the excitation source employed (5–6 mW) for NMR samples. Complex **3a** is highly symmetrical and has four resonances for the bpy ligand (9.50, 8.21, 8.12 and 7.73 ppm) and four resonances for the 4APs (7.53, 6.31, 6.25 and 5.83 ppm) with same integrated intensities. The presence of free bpy was ruled out by the comparison with the  $^1\text{H}$  spectrum of the ligand in water (peaks at 8.57, 7.96 and 7.47 ppm). The presence of only four bpy resonances and their relative intensity with respect to the 4AP signals suggests that only **3a** or the *trans* diaqua **3c** can be responsible for these signals. The unexpected 1:1 intensity ratio for the proton signals of 4APs and bpy in **3a** can be ascribed to rotational movements of the axial ancillary 4APs. It is possible to postulate a concerted rotation of the 4APs due to the very short Ru–N(bpy) distances (2.05 Å). The low concentration of this species prevented further NMR investigations of its dynamic behavior. Fitting the experimental and calculated proton chemical shifts for the bpy and 4AP resonances of **3a** and **3c** gives a better fitting in the case of the former (*R* factor = 0.96 and 0.82 respectively; see Supporting Information). Furthermore, as shown by the computed geometries, **3a** has the shortest Ru–N(bpy) distances, which can account for the significant shielding of the *ortho* protons of axial 4APs. Their computed chemical shifts seem to confirm this. The NMR signals of **3a** are sharper than those of **2a**. This fact might be related to the different exchange rates with the solvent, as expected for a mono and diaqua ruthenium complexes.<sup>70</sup> NMR spectra in NaCl solution show that coordination of free  $\text{Cl}^-$  is not taking place.

ESI mass spectra of **1** after 2 h irradiation at 510 nm in water and/or water/acetonitrile (5%) confirm the presence of monoqua and diaqua derivatives. In both solutions, a peak assignable to the species  $[\text{Ru}(\text{bpy})(4\text{AP})_4]\text{ClO}_4^+$  is present at  $m/z$  733;  $[\text{Ru}(\text{bpy})(4\text{AP})_3]^{2+}$  gives a peak at  $m/z$  270 in pure water (100 % relative abundance), while  $[\text{Ru}(\text{bpy})(4\text{AP})_3(\text{CH}_3\text{CN})]^{2+}$  appears at  $m/z$  290 in the water/acetonitrile solution (100% relative abundance). The disubstituted species  $[\text{Ru}(\text{bpy})(4\text{AP})_2(\text{H}_2\text{O})_2]^{2+}$  and  $[\text{Ru}(\text{bpy})(4\text{AP})_2(\text{CH}_3\text{CN})_2]^{2+}$  appear at  $m/z$  239 (33%) and  $m/z$  264 (10%), respectively.

Recently, Etchenique et al. have studied the related Ru complex  $[\text{Ru}(\text{bpy})(\text{CH}_3\text{CN})_4]^{2+}$ ,<sup>71</sup> which undergoes photodissociation producing, though, different isomers to **1**. This aspect can be relevant since it has been shown that isomers of the same complex may have very different DNA-binding properties in a series of anticancer compounds.<sup>72,73</sup>

**Orbital Analysis.** The electronic structure of **1** was calculated taking in account the role of the solvent since it has been demonstrated previously that solvent effects play an important role.<sup>74</sup> The three HOMOs have small energy differences, especially HOMO and HOMO–1 which are almost degenerate. The HOMO metal contribution is 67%, while the ligands contribute in an almost even way except for one equatorial 4AP which contributes 15%. The same occurs for the HOMO–1 orbital, where the metal character is increased to 71 % and there is an axial 4AP contribution of 15%.

The most important occupied orbital is HOMO–2, because of the role it plays in the singlet transition responsible for the band centered at 510 nm. The metal contribution to this orbital is 71%; a 17% contribution from an axial 4AP and 7% contribution from the bpy are present. The HOMO–2 orbital is shown in Figure 8. The other occupied orbitals lie at lower energy (0.7 eV) and they have a reduced metal character. Furthermore they have a marginal role in the excited-state properties of the complex. The lowest lying three unoccupied molecular orbitals have a high bpy character (> 93%). In the LUMO there is a 5% contribution from a metal d orbital with opposite phase to that of the  $\pi^*$  bpy orbital. The LUMO is followed in energy by two bpy-centered orbitals (0.9 eV) with different symmetry. A series of three  $\pi^*$  4AP-centered orbitals is present closely above. These orbitals have some bonding character among the axial and the equatorial 4APs and among the equatorial 4APs and the metal center. Of particular relevance for the photodissociation properties of **1** are the orbitals LUMO+11, LUMO+12 and LUMO+13. They lay within 0.05 eV and have anti-bonding features with respect to both the bpy and 4APs (Figure 8). LUMO+11 is Ru(bpy)-centered (36% Ru, 54% bpy) and has anti-bonding character on the Ru–N(bpy) and Ru–N(*eq*–4AP)

bonds. LUMO+13 is similar in shape but with a reduced Ru contribution (29%) and an increased bpy contribution (57%). LUMO+12 is different. There was a Ru contribution of 64% and only a small bpy contribution (6%). Both *axial* 4APs are strongly anti-bonding with respect to Ru–N bonds.

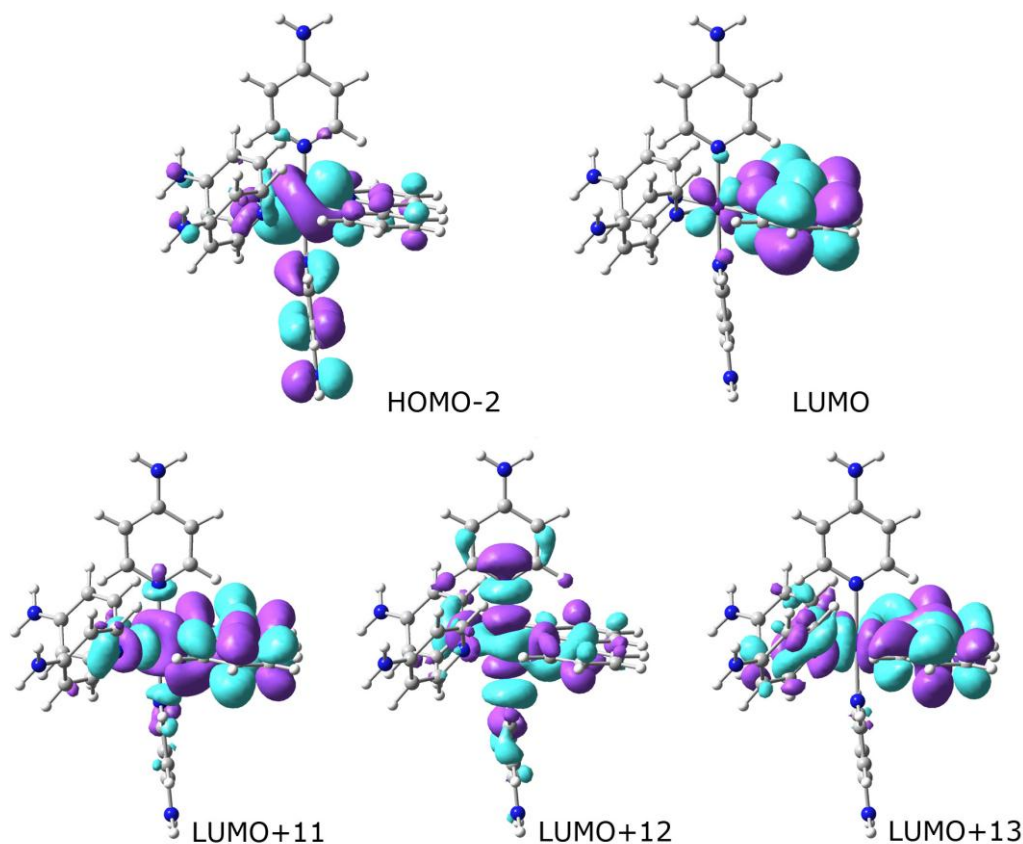


**Figure 8.** Selected molecular orbitals for complex **1**. Orbital relative energies relative to the HOMO are LUMO = 3.07 eV, LUMO+11 = 5.42 eV, LUMO+12 = 5.43 eV and LUMO+13 = 5.54 eV.

**Ru–4AP Photodissociation Mechanism.** The photochemistry of Ru(bpy) complexes has been explored extensively during the last decades. Photodissociation of ligands has been attributed to the thermal population of d–d dissociative states (generally triplets) similar in energy to the emitting MLCT states. Photodissociation quantum yields correlate with the energies of the MLCT band of the Ru complexes, their emission maxima and electrochemical potential.<sup>3,7,75,76</sup> Blue <sup>3</sup>MLCT bands are generally associated with higher photodissociation yields. In the case of [Ru(bpy)<sub>2</sub>L<sub>2</sub>]<sup>2+</sup> complexes, we recently showed that mixing between <sup>3</sup>MLCT and dissociative <sup>3</sup>MC is essential for ligand photodissociation since it allows direct population of such mixed triplet states from singlet states through intersystem crossing.<sup>21</sup>

In order to identify the relevant excited electronic states for the photodissociation of the first 4AP ligand and for confirming the results obtained spectroscopically, evolution of singlet (Figure 9) and triplet (Figure 10) excited states was monitored along the Ru–N(*axial* 4AP) and Ru–N(*equatorial* 4AP) dissociation coordinates.

**Singlet Excited States.** Irradiation of **1** with 510-nm light produces population of the singlet state **S3**. At the equilibrium geometry, **S3** has a very small LUMO+12 contribution (3%), which remains limited along the reaction coordinates. The higher-energy states, namely **S4–S8**, all have a partially dissociative character towards the 4AP ligand (<sup>1</sup>MLCT/MC). All these states have a similar shape at the equilibrium geometry, indicating that mixing is occurring. **S6** has the most dissociative character with 80% contribution from antibonding orbitals.

Along both the axial and equatorial reaction coordinates, the energy difference between **S4–S8** and **S3** is too high for causing dissociation from the singlet state. Figure 9A shows that the potential energy curve (PEC) of **S6** crosses the PEC of **S3** when the Ru–N(*axial* 4AP) distance is less than 2.57 Å. Such a crossing indicates

that dissociation from an axial 4AP is favored, however, the oscillator strength of **S6** is zero along the whole reaction coordinate indicating that **S6** is forbidden and thus not populated.

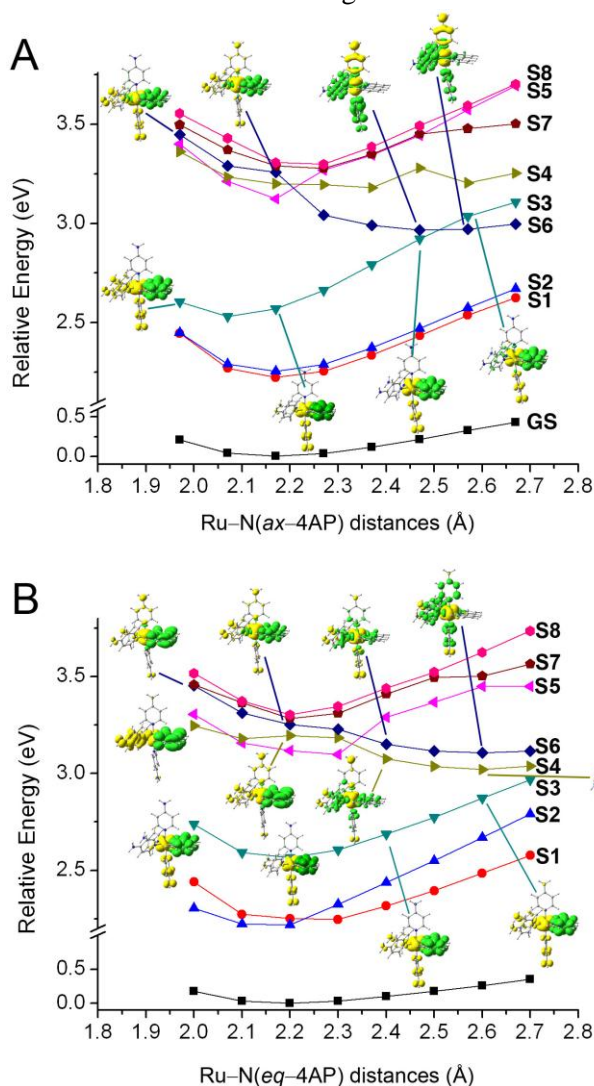


**Figure 9.** Potential energy curves of selected singlet excited states of **1** along (A) the Ru–N(*axial* 4AP) and (B) Ru–N(*equatorial* 4AP) coordinates. The zero-point of the energy scale is set to the ground-state energy at its equilibrium geometry.

**Triplet Excited States.** PECs of the lowest-energy triplet excited states along the Ru–N(*axial* 4AP) and the Ru–N(*equatorial* 4AP) axes were analyzed as well, obtaining useful insights into the ligand photodissociation mechanism.

The triplet state **T4** has dissociative character due to the contribution from LUMO+11 and LUMO+12 orbitals. For the ground-state geometry, this state is 0.86 eV above the three <sup>3</sup>MLLCT states (**T1–T3**, Figure 3). Along the Ru–N(*axial* 4AP) stretching coordinate, the dissociative triplet state does not get closer in energy to the low-lying <sup>3</sup>MLLCT states, and no contributions from the LUMO+11 or LUMO+12 are found in those states either. Moreover, other high-energy <sup>3</sup>MLLCTs move closer in energy to **T1–T3** than **T4**.

The results obtained from lengthening the bond distance along the Ru–N(*equatorial* 4AP) coordinate are different. In this case the dissociative state **T4** becomes closer in energy to **T3**, the **T4–T3** energy difference being 0.50 eV at 2.50 Å. No inter-system crossing pathways are present between **S3** and **T4**, but it is worth pointing out that **T4** acquires a significant contribution from HOMO–2, which is characteristic of **S3** and **T3**.

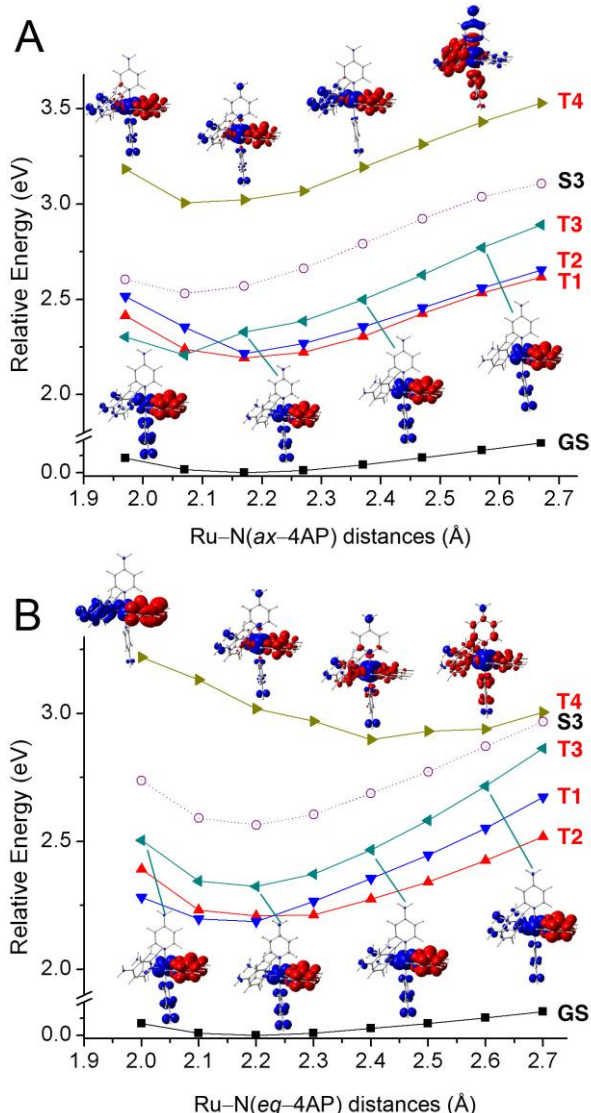


**Figure 10.** Potential energy curves of selected triplet excited states of **1** along the (A) Ru–N(*ax*–4AP) and (B) Ru–N(*eq*–4AP) coordinate. The zero-point of the energy scale is set to the ground-state energy at its equilibrium geometry.

In agreement with such result Endicott and coworkers showed that mixing between  $^3\text{MLCT}$  and  $^3\text{MC}$  states is common in  $[\text{Ru}(\text{bpy})(\text{L})_4]^{2+}$  systems and strongly affects the emission properties of such complexes.<sup>77</sup> Furthermore, the lowest-lying triplet-state geometry shows that formation of the triplet state causes elongation of both Ru–N(*equatorial* 4AP) bonds (by 0.03 Å), while one Ru–N(*axial* 4AP) bond becomes shorter (by 0.05 Å) and the other slightly longer (by 0.01 Å). Population of SOMO–1 (Figure 11), which has  $\pi^*$ -antibonding character toward three 4AP, explains such structural feature.

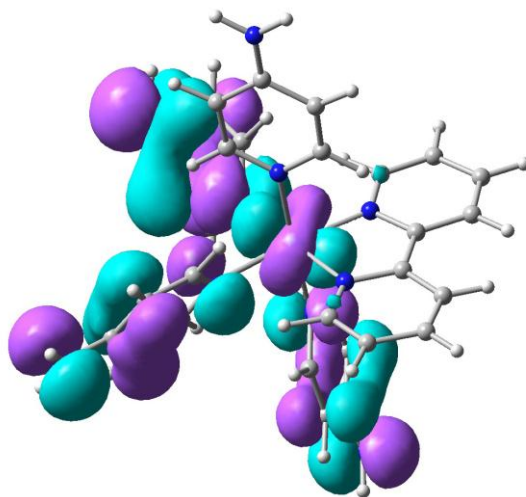


**Figure 11.** SOMO–1 orbital of **1** in the lowest-lying triplet geometry ( $T_1$ ).

## Conclusions

In this paper we have shown that the novel complex  $[\text{Ru}(\text{bpy})(4\text{AP})_4]^{2+}$  (**1**) undergoes specific and selective photocleavage of two 4AP ligands. We have determined the photodissociation quantum yields of **1** and identified the products of the light-induced reaction by NMR and mass spectrometry.

PECs calculated for elongation of the Ru–N(*axial* 4AP) and the Ru–N(*equatorial* 4AP) bond gave useful insights on the photodissociation mechanism. Upon absorption of green light, the  $^1\text{MLLCT}$  state **S3** is populated. Only hot photons can promote population of the higher-energy singlet states (**S4–S8**) having partially dissociative character. In fact, **S4–S8** remain higher in energy than **S3** along both Ru–N(*axial* 4AP) and the Ru–N(*equatorial* 4AP) reaction coordinates; the only exception is **S6** in the case of the stretching of an axial Ru–N(4AP) bond, but its oscillator strength is zero and the crossing with **S3** occurs at long Ru–N(*axial* 4AP) distances. Direct dissociation from dissociative singlet states can therefore be considered of little importance.

Photodissociation quantum yields and spectroscopic measurements indicate that the first 4AP ligand dissociates relatively slowly, at least compared to ultrafast processes such as CO dissociation from myoglobin or  $[\text{M}(\text{bpy})(\text{CO})_4]$  complexes (where M = Cr, W, Mo) and  $[\text{Ru}(\text{bpy})(\text{CO})_2\text{X}_2]$  (where X = Cl, Br and I) complexes.<sup>22–27</sup> The avoidance of crossing between the PECs of **S3** and **S4–S8** is in agreement with the small photodissociation yield in **1**. On the contrary, ultrafast and efficient reactions would show crossing points in PECs relative to singlet states.<sup>78</sup>

This fact, and the photochemical features of  $[\text{Ru}(\text{bpy})_2(\text{L})_2]^{2+}$  complexes (where L is the released ancillary ligand), suggest that triplet states are involved in the photodissociation of the first 4AP ligand. According to TDDFT calculations, this scenario seems possible only in the case of the equatorial 4AP, which confirms NMR data. In fact, only the stretching of the Ru–N(*equatorial* 4AP) bond seems able to produce some mixing between **T3** and **T4**, as shown by the shape of **T4** and by the presence of HOMO–2 contributions to **T4**. As observed previously,<sup>79</sup> the photochemistry could result from such mixing and not from direct population of a dissociative state.

For **1**, the mixing between the dissociative  $^3\text{MC}$  and  $^3\text{MLLCT}$  states is limited compared to  $[\text{Ru}(\text{bpy})_2(\text{py})_2]^{2+}$  and  $[\text{Ru}(\text{bpy})_2(4\text{AP})_2]^{2+}$ , in agreement with its lower photodissociation yield, but also its shorter Ru–N(L) distances in the lowest-lying triplet geometry. UKS calculations showed that, in the case of  $[\text{Ru}(\text{bpy})_2(\text{L})_2]^{2+}$  derivatives, the lowest-lying triplet state has an extremely long Ru–N(L) distance ( $\sim 2.70 \text{ \AA}$ ), due to  $\sigma^*$ -antibonding character of the SOMO.<sup>21</sup>

Photoactivation of metal complexes has been used to increase the reaction rate of several thermally accessible processes. However, excited-state reactions may also give unique reaction mechanisms, which lead to different transition states and thus to photoproducts otherwise not obtainable.<sup>80</sup> The control of such mechanisms in metal complexes depends on the electronic properties of the coordinated ligands. A combination of TDDFT and spectroscopic techniques is then necessary to tune the photoactivation process and design metal complexes suitable for medicinal applications.

## Acknowledgment

C. G. thanks Regione Piemonte for financial support. L. S. thanks the EU FP7 Marie Curie Action IEF 220281 PHOTORUACD for financial support. EXAFS experiments were performed at BM29 beamline of the ESRF synchrotron (experiment CH-2604). The authors acknowledge the friendly and highly competent support of C. Prestipino during the EXAFS data collection. We are indebted with Dr. E. Groppo for fruitful discussions.

**Supporting Information Available:**  $^1\text{H}$ - $^1\text{H}$  COSY and  $^1\text{H}$ - $^1\text{H}$  NOESY of **1**, DFT/GIAO NMR chemical shift data for **1** and its photoderivatives, TDDFT singlet excited-state data, theoretical description of consecutive two-step photocleavage, raw EXAFS data collected in both fluorescence and transmission modes, full reference 29.<sup>35</sup> This material is free of charge via the Internet at <http://pubs.acs.org>.

## References

1. Mackay, F. S.; Woods, J. A.; Heringová, P.; Kašpárková, J.; Pizarro, A. M.; Moggach, S. A.; Parsons, S.; Brabec, V.; Sadler, P. J. *Proc. Natl. Acad. Sci. U. S. A.* **2007**, 104, 20743–20748.
2. Bednarski, P. J.; Grunert, R.; Zielzki, M.; Wellner, A.; Mackay, F. S.; Sadler, P. J. *Chemistry & Biology* **2006**, 13, 61–67.
3. Zayat, L.; Calero, C.; Albores, P.; Baraldo, L.; Etchenique, R. *J. Am. Chem. Soc.* **2003**, 125, 882–883.
4. Zayat, L.; Salierno, M.; Etchenique, R. *Inorg. Chem.* **2006**, 45, 1728–1731.
5. Salierno, M.; Fameli, C.; Etchenique, R. *Eur. J. Inorg. Chem.* **2008**, 1125–1128.
6. Mackay, F. S.; Woods, J. A.; Moseley, H.; Ferguson, J.; Dawson, A.; Parsons, S.; Sadler, P. J. *Chem. - Eur. J.* **2006**, 12, 3155–3161.
7. Pinnick, D. V.; Durham, B. *Inorg. Chem.* **1984**, 23, 1440–1445.
8. Nikolenko, V.; Yuste, R.; Zayat, L.; Baraldo, L. M.; Etchenique, R. *Chem. Commun.* **2005**, 1752–1754.
9. Brancaleon, L.; Moseley, H. *Lasers Med. Sci.* **2002**, 17, 173–186.
10. Karidi, K.; Garoufis, A.; Tsipis, A.; Hadjiliadis, N.; den Dulk, H.; Reedijk, J. *Dalton Trans.* **2005**, 1176–1187.
11. Vlček, A.; Zálšíš, S. *Coord. Chem. Rev.* **2007**, 251, 258–287.
12. Salassa, L.; Garino, C.; Albertino, A.; Volpi, G.; Nervi, C.; Gobetto, R.; Hardcastle, K. I. *Organometallics* **2008**, 27, 1427–1435.
13. Garino, C.; Rui, T.; Salassa, L.; Albertino, A.; Volpi, G.; Nervi, C.; Gobetto, R.; Hardcastle, K. I. *Eur. J. Inorg. Chem.* **2008**, 3587–3591.
14. Albertino, A.; Garino, C.; Ghiani, S.; Gobetto, R.; Nervi, C.; Salassa, L.; Rosenberg, E.; Sharmin, A.; Viscardi, G.; Buscaino, R.; Croce, G.; Milanese, M. *J. Organomet. Chem.* **2007**, 692, 1377–1391.
15. De Angelis, F.; Fantacci, S.; Selloni, A.; Nazeeruddin, M. K.; Grätzel, M. *J. Am. Chem. Soc.* **2007**, 129, 14156–14157.



16. Di Censo, D.; Fantacci, S.; De Angelis, F.; Klein, C.; Evans, N.; Kalyanasundaram, K.; Bolink, H. J.; Grätzel, M.; Nazeeruddin, M. K. *Inorg. Chem.* **2008**, 47, 980–989.
17. Labat, F.; Laine, P. P.; Ciofini, I.; Adamo, C. *Chem. Phys. Lett.* **2006**, 417, 445–451.
18. Laine, P. P.; Ciofini, I.; Ochsenbein, P.; Amouyal, E.; Adamo, C.; Bedioui, F. *Chem. -Eur. J.* **2005**, 11, 3711–3727.
19. Ciofini, I.; Laine, P. P.; Bedioui, F.; Adamo, C. *J. Am. Chem. Soc.* **2004**, 126, 10763–10777.
20. Guillemoles, J. F.; Barone, V.; Joubert, L.; Adamo, C. *J. Phys. Chem. A* **2002**, 106, 11354–11360.
21. Salassa, L.; Garino, C.; Salassa, G.; Gobetto, R.; Nervi, C. *J. Am. Chem. Soc.* **2008**, 130, 9590–9597.
22. De Angelis, F.; Car, R.; Spiro, T. G. *J. Am. Chem. Soc.* **2003**, 125, 15710–15711.
23. Guillaumont, D.; Vlček, A.; Daniel, C. *J. Phys. Chem. A* **2001**, 105, 1107–1114.
24. Daniel, C. *Coord. Chem. Rev.* **2003**, 238, 143–166.
25. Vlček, A. *Coord. Chem. Rev.* **1998**, 177, 219–256.
26. Gabrielsson, A.; Zališ, S.; Matousek, P.; Towrie, M.; Vlček, A. *Inorg. Chem.* **2004**, 43, 7380–7388.
27. Dunietz, B. D.; Dreuw, A.; Head-Gordon, M. *J. Phys. Chem. B* **2003**, 107, 5623–5629.
28. Ciofini, I.; Daul, C. A.; Adamo, C. *J. Phys. Chem. A* **2003**, 107, 11182–11190.
29. Dreuw, A.; Dunietz, B. D.; Head-Gordon, M. *J. Am. Chem. Soc.* **2002**, 124, 12070–12071.
30. Amarengo, W. L. F.; Perrin, D. D. *Purification of Laboratory Chemicals*; 4th Ed. ed.; Butterworth-Heinemann: Oxford, 1996.
31. Kim, B. H.; Lee, D. N.; Park, H. J.; Min, J. H.; Jun, Y. M.; Park, S. J.; Lee, W. Y. *Talanta* **2004**, 62, 595–602.
32. Filipponi, A.; Borowski, M.; Bowron, D. T.; Ansell, S.; Di Cicco, A.; De Panilis, S.; Itie, J. P. *Rev. Sci. Instrum.* **2000**, 71, 2422–2432.
33. Ravel, B.; Newville, M. J. *J. Synchrotr. Radiat.* **2005**, 12, 537–541.
34. Ankudinov, A. L.; Ravel, B.; Rehr, J. J.; Conradson, S. D. *Phys. Rev. B* **1998**, 58, 7565–7576.
35. Frisch, M. et al. *Gaussian 03*, revision D 0.1; Gaussian Inc.: Wallingford CT, 2004.
36. Becke, A. D. *J. Chem. Phys.* **1993**, 98, 5648–5652.
37. Lee, C.; Yang, W.; Parr, R. G. *Phys. Rev. B: Condens. Matter* **1988**, 37, 785–789.
38. Hay, P. J.; Wadt, W. R. *J. Chem. Phys.* **1985**, 82, 270–283.
39. McLean, A. D.; Chandler, G. S. *J. Chem. Phys.* **1980**, 72, 5639–5648.
40. Cossi, M.; Rega, N.; Scalmani, G.; Barone, V. *J. Comput. Chem.* **2003**, 24, 669–681.
41. Cossi, M.; Barone, V. *J. Chem. Phys.* **2001**, 115, 4708–4717.
42. Barone, V.; Cossi, M. *J. Phys. Chem. A* **1998**, 102, 1995–2001.
43. Casida, M. E.; Jamorski, C.; Casida, K. C.; Salahub, D. R. *J. Chem. Phys.* **1998**, 108, 4439–4449.
44. Stratmann, R. E.; Scuseria, G. E.; Frisch, M. J. *J. Chem. Phys.* **1998**, 109, 8218–8224.
45. Browne, W. R.; O'Boyle, N. M.; McGarvey, J. J.; Vos, J. G. *Chem. Soc. Rev.* **2005**, 34, 641–663.
46. O'Boyle, N. M.; Vos, J. G. *GaussSum*, version 1.0.5; Dublin City University. Available at <http://gausssum.sourceforge.net>, 2005.
47. Villegas, J. M.; Stoyanov, S. R.; Huang, W.; Rillema, P. D. *Inorg. Chem.* **2005**, 44, 2297–2309.
48. Stoyanov, S. R.; Villegas, J. M.; Cruz, A. J.; Lockyear, L. L.; Reibenspies, J. H.; Rillema, P. D. *J. Chem. Theory Comput.* **2005**, 1, 95–106.
49. Helgaker, T.; Jaszunski, M.; Ruud, K. *Chem. Rev.* **1999**, 99, 293–352.
50. Gawelda, W.; Johnson, M.; de Groot, F. M. F.; Abela, R.; Bressler, C.; Chergui, M. *J. Am. Chem. Soc.* **2006**, 128, 5001–5009.
51. Rillema, D. P.; Jones, D. S.; Levy, H. A. *J. Chem. Soc., Chem. Commun.* **1979**, 849–851.
52. Rillema, D. P.; Jones, D. S.; Woods, C.; Levy, H. A. *Inorg. Chem.* **1992**, 31, 2935–2938.
53. This behavior seems to be typical of the EXAFS technique. When several neighbors of the same chemical nature are located at close distances, there is a tendency to let the such distances to converge to a common value, see B Bonino, F.; Chavan, S.; Vitillo, J. G.; Groppo, E.; Agostini, G.; Lamberti, C.; Dietzel, P. D. C.; Prestipino, C.; Bordiga, S. *Chem. Mat.* **2008**, 20, 4957–4968.

54. Makedonas, C.; Mitsopoulou, C. A. *Eur. J. Inorg. Chem.* **2007**, 110–119.
55. Vlček, A. *Coord. Chem. Rev.* **2002**, 230, 225–242.
56. Endicott, J. F.; Chen, Y.-J. *Coord. Chem. Rev.* **2007**, 251, 328–350.
57. Chen, Y.-J.; Xie, P.; Heeg, M. J.; Endicott, J. F. *Inorg. Chem.* **2006**, 45, 6282–6297.
58. Xie, P.; Chen, Y.-J.; Uddin, M. J.; Endicott, J. F. *J. Phys. Chem. A* **2005**, 109, 4671–4689.
59. Seneviratne, D. S.; Uddin, M. J.; Swayambunathan, V.; Schlegel, H. B.; Endicott, J. F. *Inorg. Chem.* **2002**, 41, 1502–1517.
60. Koch, W.; Holthausen, M. C. *A Chemist's Guide to DFT*; 2nd ed.; Wiley-VCH: Weinheim, 2001.
61. Polson, M.; Ravaglia, M.; Fracasso, S.; Garavelli, M.; Scandola, F. *Inorg. Chem.* **2005**, 44, 1282–1289.
62. Munzarova, M. L.; Kubáček, P.; Kaupp, M. *J. Am. Chem. Soc.* **2000**, 122, 11900–11913.
63. Novozhilova, I. V.; Volkov, A. V.; Coppens, P. *J. Am. Chem. Soc.* **2003**, 125, 1079–1087.
64. Ruiz, E.; Cirera, J.; Alvarez, S. *Coord. Chem. Rev.* **2005**, 249, 2649–2660.
65. Adamo, C.; Subra, R.; Di Matteo, A.; Barone, V. *J. Chem. Phys.* **1998**, 109, 10244–10254.
66. Brown, E. B.; Shear, J. B.; Adams, S. R.; Tsien, R. Y.; Webb, W. W. *Biophys. J.* **1999**, 76, 489–499.
67. Digman, M. A.; Sengupta, P.; Wiseman, P. W.; Brown, C. M.; Horwitz, A. R.; Gratton, E. *Biophys. J.* **2005**, 88, L33–L36.
68. Gobetto, R.; Nervi, C.; Romanin, B.; Salassa, L.; Milanesio, M.; Croce, G. *Organometallics* **2003**, 22, 4012–4019.
69. Velders, A. H.; Massera, C.; Ugozzoli, F.; Biagini-Cingi, M.; Manotti-Lanfredi, A. M.; Haasnoot, J. G.; Reedijk, J. *Eur. J. Inorg. Chem.* **2002**, 193–198.
70. Helm, L.; Merbach, A. E. *Chem. Rev.* **2005**, 105, 1923–1959.
71. Petroni, A.; Slep, L. D.; Etchenique, R. *Inorg. Chem.* **2008**, 47, 951–956.
72. Hotze, A. C. G.; Caspers, S. E.; de Vos, D.; Kooijman, H.; Spek, A. L.; Flamigni, A.; Bacac, M.; Sava, G.; Haasnoot, J. G.; Reedijk, J. J. *Biol. Inorg. Chem.* **2004**, 9, 354–364.
73. Nováková, O.; Kašpárková, J.; Vrána, O.; Vanvliet, P. M.; Reedijk, J.; Brabec, V. *Biochemistry* **1995**, 34, 12369–12378.
74. Fantacci, S.; De Angelis, F.; Selloni, A. *J. Am. Chem. Soc.* **2003**, 125, 4381–4387.
75. Collin, J. P.; Jouvenot, D.; Koizumi, M.; Sauvage, J. P. *Inorg. Chem.* **2005**, 44, 4693–4698.
76. Pinnick, D. V.; Durham, B. *Inorg. Chem.* **1984**, 23, 3841–3842.
77. Odongo, O. S.; Heeg, M. J.; Chen, Y. J.; Xie, P. H.; Endicott, J. F. *Inorg. Chem.* **2008**, 47, 7493–7511.
78. Dreuw, A.; Head-Gordon, M. *Coord. Chem. Rev.* **2005**, 105, 4009–4037.
79. Wilson, R. B.; Solomon, E. I. *J. Am. Chem. Soc.* **1980**, 102, 4085–4095.
80. Kojima, T.; Sakamoto, T.; Matsuda, Y. *Inorg. Chem.* **2004**, 43, 2243–2245.